
Representation Theoretic Patterns in Multi-Frequency Class Averaging for Three-Dimensional Cryo-Electron Microscopy

Tingran Gao · Yifeng Fan · Zhizhen Zhao

Received: date / Accepted: date

Abstract We develop in this paper a novel intrinsic classification algorithm — *multi-frequency class averaging* (MFCA) — for clustering noisy projection images obtained from three-dimensional cryo-electron microscopy (cryo-EM) by the similarity among their viewing directions. This new algorithm leverages multiple irreducible representations of the unitary group to introduce additional redundancy into the representation of the transport data, extending and outperforming the previous class averaging algorithm of Hadani and Singer [*Foundations of Computational Mathematics*, 11 (5), pp. 589–616 (2011)] that uses only a single representation. The formal algebraic model and representation theoretic patterns of the proposed MFCA algorithm extend the framework of Hadani and Singer to arbitrary irreducible representations of the unitary group. We conceptually establish the consistency and stability of MFCA by inspecting the spectral properties of a generalized localized parallel transport operator on the two-dimensional unit sphere through the lens of Wigner matrices. We demonstrate the efficacy of the proposed algorithm with numerical experiments.

Keywords Representation theory · Spectral theory · Differential geometry · Wigner matrices · Cryo-electron microscopy · Mathematical biology

Mathematics Subject Classification (2010) 20G05 · 33C45 · 33C55 · 55R25

1 Introduction

The past decades have witnessed an emerging and continued impact of cryo-electron microscopy (cryo-EM), the Nobel Prize winning imaging technology for determining three-dimensional structures of macromolecules,

This material is based upon work supported by the National Science Foundation under Grant No. DMS-1439786 while the first author was in residence at the Institute for Computational and Experimental Research in Mathematics (ICERM) in Providence, RI, during the Spring 2018 semester. TG acknowledges support from an AMS-Simons Travel Grant and partial support from DARPA D15AP00109 and NSF IIS 1546413.

Tingran Gao
Committee on Computational and Applied Mathematics
Department of Statistics
University of Chicago
E-mail: tingrangao@galton.uchicago.edu

Yifeng Fan
Department of Electrical and Computer Engineering
University of Illinois at Urbana–Champaign
E-mail: yifengf2@illinois.edu

Zhizhen Zhao
Department of Electrical and Computer Engineering
Coordinated Science Laboratory
University of Illinois at Urbana–Champaign
E-mail: zhizhenz@illinois.edu

on a wide range of natural scientific fields [19, 48, 28, 41, 14, 52]. Compared with its predecessor, X-ray crystallography, of which the success builds upon the potentially difficult procedure of crystallization, cryo-EM produces large numbers of projection images for samples of identical molecules rapidly immobilized in a thin layer of vitreous ice. The projection images can be thought of as tomographic projections of many copies of an identical molecule, but with unknown and random projection directions (*viewing directions*). A major computational challenge in reconstructing the three-dimensional molecular structure from these projection images is the extremely low signal-to-noise ratio (SNR) caused by the limited allowable electron dose (so as to avoid damaging the molecule before the imaging completes). It is thus customary to improve the SNR by performing *class averaging* — the procedure of aligning and then averaging out projection images taken along nearby viewing directions — from rotationally invariant pairwise comparisons of the projection images [53, 28], before the downstream reconstruction workflow such as angular reconstitution [65, 40, 56].

In addition to its scientific value, the rich geometric structure in the cryo-EM imaging model has also inspired many mathematical and algorithmic investigations [61, 59, 62, 5, 67, 10, 31, 4, 32, 68, 33]. This paper stems from our attempt at extending the representation theoretic framework of [38, 39] to account for recent progress on utilizing multiple irreducible representations for phase synchronization [34] and manifold learning [26, 27]. In a nutshell, the representation theoretic framework for class averaging [39] is centered at an integral operator (*localized parallel transport operator*) acting on sections of a complex line bundle over the two-dimensional unit sphere S^2 in \mathbb{R}^3 . This line bundle is identified with a vector bundle associated with $\text{SO}(3)$, viewed as a principal $\text{SO}(2)$ -bundle over S^2 , through the unitary irreducible representation $[0, 2\pi) \ni \theta \mapsto e^{i\theta} \in \mathbb{C}^*$.¹ In this paper, we consider an extension of this framework to other complex line bundles on S^2 , induced from the same principal bundle $\text{SO}(2) \hookrightarrow \text{SO}(3) \rightarrow S^2$ by other unitary irreducible representations of character $k \geq 1$, namely, $\rho_k : [0, 2\pi) \ni \theta \mapsto e^{ik\theta} \in \mathbb{C}^*$. This requires us to extend the *intrinsic model* of [39] to account for a general irreducible representation of $\text{U}(1)$, and to study the spectral properties of the new integral operator on the new line bundles associated with these irreducible representations. The computation involving generating functions becomes quickly infeasible if one follows the original approach of [39] in our new setting. To tackle this technical difficulty, we resort to more direct and explicit constructions of the algebraic model by means of the well-studied *Wigner matrices* in mathematical physics, which provides simplified proofs even in the original, single-frequency setting of [39]. As pointed out in [34], the multi-frequency approach essentially utilizes the additional consistency constraints across representations, and can potentially be beneficial even without introducing separate, independent measurements for the additional channels — in other words, it is possible to artificially “manufacture” representations of the data in multiple frequencies from measurements conducted in a single frequency, yet still leverage the additional redundancy in the data representation to achieve improved statistical power than the one-frequency approach. This somewhat surprising phenomenon in class averaging is the theme of our investigation in this paper.

1.1 Background: The Mathematical Model of Cryo-Electron Microscopy and Class Averaging

Following [39], we view the collection of projection images $\{I_i \in \mathbb{R}^{L \times L} \mid i = 1, \dots, N\}$ as tomographic projection images for the same three-dimensional object along projection directions uniformly sampled from the projective space S^2 , as it is more convenient to consider the imaging model in the molecule’s own lab frame, where the molecule is fixed and observed by an electron microscope at various orientations. For simplicity, we assume the projection images are all centered, i.e. the center of mass of the clean projection images are at the center of the images. The goal is to identify and cluster projection images produced from similar projection directions, hereafter referred to as *viewing directions*.

We focus on the unit sphere S^2 in \mathbb{R}^3 , and view $\text{SO}(3)$ as the frame bundle of S^2 . A point $x \in \text{SO}(3)$ is identified with an orthonormal basis $(\mathbf{e}_1, \mathbf{e}_2, \mathbf{e}_3)$ of \mathbb{R}^3 , with orientation compatible with the canonical orthonormal coordinate frame of \mathbb{R}^3 . We identify $\mathbf{e}_3 \in S^2$ with the viewing direction and denote it for $\pi(x)$ for the ease of notations. The 2D image obtained by the microscope observed at a spatial orientation x is a

¹ Throughout this paper, we will identify $\text{SO}(2) \cong \text{U}(1)$ and denote $i = \sqrt{-1}$ for the complex unit. We refer to the parameter k — the character of the irreducible representation — as the “frequency” due to its obvious connection with Fourier analysis.

real valued function $I : \mathbb{R}^2 \rightarrow \mathbb{R}$, given by the X-ray transform along the viewing direction:

$$I(s, t) = \int_{\mathbb{R}} \phi(s\mathbf{e}_1 + t\mathbf{e}_2 + r\mathbf{e}_3) dr \quad \text{for all } (s, t) \in \mathbb{R}^2 \quad (1)$$

where $\phi : \mathbb{R}^3 \rightarrow \mathbb{R}$ is a real-valued function modeling the electromagnetic potential induced from the charges of the molecule. We assume the images $I(s, t)$ are all supported on a bounded set of \mathbb{R}^2 which fits into the size of the projection images.

To measure the similarity between any two projection images I_i and I_j , obtained by the tomographic projection along viewing directions $\pi(x_i) \in S^2$ and $\pi(x_j) \in S^2$ respectively, we compute a rotationally invariant distance between I_i and I_j defined as

$$d_{\text{RID}}(I_i, I_j) = \min_{\theta \in [0, 2\pi)} \|I_i - R_\theta(I_j)\|_{\text{F}}, \quad (2)$$

where $R_\theta(I_j)$ stands for the operation of rotating image I_j by an angle $\theta \in [0, 2\pi)$ in the counterclockwise orientation, and $\|\cdot\|_{\text{F}}$ is the matrix Frobenius norm. The optimal alignment angle between I_i and I_j will be denoted as

$$\theta_{ij} = \arg \min_{\theta \in [0, 2\pi)} \|I_i - R_\theta(I_j)\|_{\text{F}}. \quad (3)$$

For images I_x and I_y obtained from viewing directions $\pi(x)$ and $\pi(y)$ for $x, y \in \text{SO}(3)$ and without noise contamination, [39] models the optimal alignment angle as the *transport data* encoding the angle of in-plane rotation needed to align frames x, y after one of them is parallel-transported to the fibre of the other using the canonical Levi-Civita connection on the unit sphere equipped with an induced Riemannian structure from the ambient space \mathbb{R}^3 . Following the convention of [39], we denote the transport data between $x, y \in \text{SO}(3)$ by $T(x, y)$, the unique $\text{SO}(2)$ element satisfying

$$x \triangleleft T(x, y) = t_{\pi(x), \pi(y)} y, \quad (4)$$

where $t_{\pi(x), \pi(y)}$ is the parallel transport along the unique geodesic on S^2 connecting $\pi(y)$ to $\pi(x)$. The optimal alignment angle θ_{ij} computed from (3) can be used to construct an approximation of the transport data between x_i and x_j (the viewing directions of I_i and I_j , respectively), at the presence of measurement and discretization error, by

$$\tilde{T}(x_i, x_j) := e^{t\theta_{ij}}. \quad (5)$$

We refer to the $\tilde{T}(x_i, x_j)$'s as the *empirical transport data*. As shown in [39], $T(x, y)$ satisfy the following properties:

$$T(x, y) = T(y, x)^{-1}, \quad \forall x, y \in S^2 \quad (\text{Symmetry})$$

$$T(g \triangleright x, g \triangleright y) = T(x, y), \quad \forall x, y \in S^2, \forall g \in \text{SO}(3) \quad (\text{Invariance})$$

$$T(x \triangleleft h_1, y \triangleleft h_2) = h_1^{-1} T(x, y) h_2, \quad \forall x, y \in S^2, \forall h_1, h_2 \in \text{SO}(2). \quad (\text{Equivariance})$$

If $\rho : \text{SO}(2) \rightarrow \mathbb{C}$ is any unitary representation of $\text{SO}(2)$ on \mathbb{C} , then the three properties above can also be cast into

$$\rho(T(x, y)) = \overline{\rho(T(y, x))}, \quad \forall x, y \in S^2 \quad (\text{Symmetry})$$

$$\rho(T(g \triangleright x, g \triangleright y)) = \rho(T(x, y)), \quad \forall x, y \in S^2, \forall g \in \text{SO}(3) \quad (\text{Invariance})$$

$$\rho(T(x \triangleleft h_1, y \triangleleft h_2)) = \overline{\rho(h_1)} \rho(T(x, y)) \rho(h_2), \quad \forall x, y \in S^2, \forall h_1, h_2 \in \text{SO}(2). \quad (\text{Equivariance})$$

We shall only assume the symmetry to be strictly satisfied by the empirical transport data; the other properties will be assumed to hold only approximately. To simplify notations, we denote for any $k \in \mathbb{Z}$

$$T^{(k)}(x, y) := \rho_k(T(x, y)), \quad \forall x, y \in \text{SO}(3) \quad (6)$$

where $\rho_k : \text{SO}(2) \rightarrow \mathbb{C}$ is the unique unitary irreducible representation of $\text{SO}(2)$ with character $k \in \mathbb{Z}$. The corresponding notation for the empirical transport data is $\tilde{T}^{(k)}(x_i, x_j)$.

In any of these irreducible representations, the empirical transport data $\{\tilde{T}^{(k)}(x_i, x_j) \mid 1 \leq i, j \leq N\}$ approximate the ground truth transport data $\{T(x_i, x_j) \mid 1 \leq i, j \leq N\}$ only when the viewing directions $\pi(x_i)$ and $\pi(x_j)$ are close to each other, in the sense that the vectors $\pi(x_i)$ and $\pi(x_j)$ belong to some small spherical cap of opening angle $a \in [0, 2\pi)$. A rough idea for filtering out far-apart viewing directions is through thresholding the rotationally invariant distances between pairs of projection images against a preset threshold parameter $\epsilon > 0$ that should be tuned to reflect the confidence in the accuracy of the imaging process. The pairwise comparison information after thresholding can be conveniently encoded into an *observation graph* $G = (V, E)$, where each vertex of G stands for one of the projection images, and an edge (i, j) belongs to the edge set E if and only if the rotationally invariant distance $d_{\text{RID}}(I_i, I_j)$ is smaller than the threshold. In an ideal noiseless world, the geometry of the graph G is a neighborhood graph on the unit sphere S^2 , namely, two images are connected if and only if their viewing directions $\pi(x_i)$ and $\pi(x_j)$ are close on the unit sphere, $(\pi(x_i), \pi(x_j)) \geq 1 - h$, for $h \ll 1$. From the noisy cryo-EM images, the rotationally invariant distances d_{RID} are affected by noise and d_{RID} -based similarity measure will connect images of very different views, introducing short-cut edges on the unit sphere. The main problem here is thus to distinguish the “good” edges from the “bad” ones in the graph G , or, in other words, to distinguish the true neighbors from the outliers. The existence of outliers makes the classification problem non-trivial. Without excluding the outliers, averaging rotationally aligned images with small invariant distance (2) yields a poor estimate of the true signal, rendering infeasible the 3D *ab initio* reconstruction from denoised images. We refer interested readers to [22, 47] for more detailed statistical analysis of the rotationally invariant distance (2). The focus of this paper is to rectify the noise-contaminated empirical transport data using the spectral information of an integral operator constructed from the local transport data, detailed in the remainder of this section.

1.1.1 The Class Averaging Algorithm

One of the most natural ideas for performing class averaging is through the eigenvectors of the class averaging matrix constructed from the empirical transport data [63]. We briefly recapture the main steps in the class averaging algorithm below. Detailed discussions and the analysis of representation theoretical patterns can be found in [63, 39]. In this section we use notation $[N] = \{1, 2, \dots, N\}$ for $N \in \mathbb{N}$.

The algorithm begins with computing rotationally invariant distances d_{ij} between all pairs of projection images I_i and I_j , along with the corresponding optimal alignment angles θ_{ij} . After that, construct N -by- N Hermitian matrix H by

$$H_{ij} = \begin{cases} e^{i\theta_{ij}} & \text{if } (i, j) \in E \\ 0 & \text{otherwise} \end{cases}$$

where the edge set $E \subset [N] \times [N]$ is obtained by thresholding the pairwise distances $\{d_{ij} : 1 \leq i, j \leq N\}$, i.e., $(i, j) \in E$ if and only if d_{ij} is below a preset threshold $\epsilon > 0$, i.e.,

$$E := \{(i, j) \in [N] \times [N] : d_{\text{RID}}(I_i, I_j) < \epsilon\}. \quad (7)$$

Set D as the diagonal matrix with diagonal entries

$$D_{ii} = \sum_{j=1}^N |H_{ij}|, \quad 1 \neq i \leq N \quad (8)$$

and compute the top three eigenvectors $\psi_1, \psi_2, \psi_3 \in \mathbb{C}^N$ of the normalized Hermitian matrix

$$\tilde{H} := D^{-1/2} H D^{-1/2}.$$

Each projection image is then associated with a point in \mathbb{C}^3 by means of the embedding map

$$\begin{aligned} \Psi : \{I_i\}_{i=1}^N &\longrightarrow \mathbb{C}^3 \\ I_i &\longmapsto (\psi_1(i), \psi_2(i), \psi_3(i)) \end{aligned}$$

where $\psi_1(i), \psi_2(i), \psi_3(i)$ denotes for the i th entries of ψ_1, ψ_2, ψ_3 , respectively. The measure of affinity between I_i and I_j is then computed using the embedding map Ψ :

$$A_{ij} := \frac{|\langle \Psi(I_i), \Psi(I_j) \rangle|}{\|\Psi(I_i)\| \|\Psi(I_j)\|}, \quad 1 \leq i \neq j \leq N. \quad (9)$$

Finally, the neighbors of a projection image I_i is determined by thresholding the affinity measures G_{ij} :

$$\text{Neighbors of } I_i := \{I_j \mid A_{ij} > 1 - \gamma\}$$

where $0 < \gamma < 1$ is another preset threshold parameter that controls the size of the neighborhoods.

We will use the shorthand notation $\mathcal{H} = \mathbb{C}(X)$ for the Hilbert space of smooth complex valued functions on $\text{SO}(3)$, with standard Hermitian inner product

$$\langle f_1, f_2 \rangle_{\mathcal{H}} = \int_{S^2} f_1(x) \overline{f_2(x)} dx, \quad f_1, f_2 \in \mathcal{H}. \quad (10)$$

Here dx denotes the normalized Haar measure on S^2 . In [63, 39], it was argued that the Hermitian matrix H containing the unitary irreducible representation of the local empirical transport data should be understood as the discretization (under uniform random sampling on $\text{SO}(3)$) of an integral operator $T_h : \mathcal{H} \rightarrow \mathcal{H}$ defined as

$$(T_h s)(x) := \int_{B(x,a)} T(x,y) s(y) dy, \quad \text{for all } s \in \mathcal{H} \quad (11)$$

where $h = 1 - \cos a$ is the locality (bandwidth) parameter. Consequently, many properties of the local transport data matrix H can be studied through its ‘‘continuous limit’’ T_h , especially the eigenvalues and eigenvectors, which converge to the eigenvalues and eigenfunctions of T_h in an appropriate sense [44]; this perspective is common in the manifold learning literature [6, 7, 16, 62, 32]. In the class averaging setting, the integral operator T_h enjoys many useful invariance and equivariance properties, which makes it relatively straightforward to study its spectral data using representation theoretic tools. Hadani and Singer noticed that T_h acts on the subspace \mathcal{H}_{-1} of \mathcal{H} consisting of *spin-weighted spherical harmonics* of $\text{SO}(3)$ of weight $s = -1$, defined as

$$\mathcal{H}_{-1} := \{s \in \mathcal{H} \mid s(e^{i\theta}x) = e^{-i\theta} s(x) \text{ for all } x \in \text{SO}(3)\}. \quad (12)$$

The space \mathcal{H}_{-1} is also canonically identified with the linear space of sections of a complex line bundle over $\text{SO}(3)$ induced by the unitary irreducible representation of $\text{U}(1)$ with character $k = 1$ [36, 13, 11, 21, 50, 49]. Furthermore, T_h commutes with the induced left action of $\text{SO}(3)$ on \mathcal{H}_{-1} , which by Schur’s theorem indicates that the eigenspaces of T_h coincides with the isotypic components of \mathcal{H}_{-1} under the left $\text{SO}(3)$ action. In particular, this mechanism can be used to show that the top eigenspace of T_h is the unique isotypic component of \mathcal{H}_{-1} corresponding to the unique three-dimensional unitary irreducible representation of $\text{SO}(3)$ for all sufficiently small $h > 0$, and that the affinity measure G_{ij} is exactly identical with the cosine value of the viewing angle between I_i and I_j in the noise-free setting.

1.1.2 Multi-Frequency Class Averaging (MFCA)

Motivated by recent work [4, 34, 26, 27] extending the synchronization approach to incorporate multiple representations of the pairwise comparison information into a unified computational framework, we propose in this paper a *multi-frequency class averaging* algorithm that creates more than one copies of the class averaging matrix — one for each ‘‘frequency channel’’ corresponding to one irreducible representation of $\text{SO}(2)$ — and then aggregate the affinity measures across the frequency channels. In the clean, noiseless scenario, the multi-frequency class averaging matrices certainly carry identical information for exactly recovering the affinity among view directions of the projection images; the real advantage, as argued and demonstrated in the theoretical analysis of [34] and the experimental results of [26, 27], lies at the low SNR region where utilizing higher-moment information becomes particularly beneficial even without introducing additional independent measurements for those higher moments.

Throughout our discussion involving multiple frequency channels, we will fix an integer $k_{\max} \geq 1$ for the total number of frequency channels considered. For each frequency $k = 1, \dots, k_{\max}$, we construct a separate class averaging matrix by

$$H_{ij}^{(k)} = \begin{cases} e^{ik\theta_{ij}} & \text{if } (i, j) \in E \\ 0 & \text{otherwise} \end{cases} \quad (13)$$

In view of (6), the Hermitian matrix $H^{(k)}$ stores the transport data under the k th irreducible representation of $\text{SO}(2)$. We then normalize each $H^{(k)}$ using the same degree matrix D as in (8); note that all matrices $H^{(k)}$ share the same sparsity pattern determined by E . After performing eigen-decomposition for $\tilde{H} = D^{-1/2}H^{(k)}D^{-1/2}$, we keep the top $(2k+1)$ eigenvectors $\psi_1^{(k)}, \dots, \psi_{2k+1}^{(k)} \in \mathbb{C}^N$ and define embedding

$$\begin{aligned} \Psi^{(k)} : \{I_i\}_{i=1}^N &\longrightarrow \mathbb{C}^{2k+1} \\ I_i &\longmapsto \left(\psi_1^{(k)}(I_i), \dots, \psi_{2k+1}^{(k)}(I_i) \right) \end{aligned} \quad (14)$$

with which we compute the affinity measure between I_i and I_j at frequency k as

$$A_{ij}^{(k)} := \frac{|\langle \Psi^{(k)}(I_i), \Psi^{(k)}(I_j) \rangle|}{\|\Psi^{(k)}(I_i)\| \|\Psi^{(k)}(I_j)\|}, \quad 1 \leq i \neq j \leq N. \quad (15)$$

Obviously, $\Psi^{(1)} = \Psi$ and $A_{ij}^{(1)} = A_{ij}$. We can either perform nearest neighbor search using the affinity measure $A_{ij}^{(k)}$ computed from an individual frequency k , or using an aggregated affinity measure such as

$$A_{ij}^{\text{All}} := \prod_{k=1}^{k_{\max}} A_{ij}^{(k)}. \quad (16)$$

The rationale behind the specific forms of (14), (15), and (16) is the core of this paper. In a nutshell, we use a $(2k+1)$ -dimensional embedding because by Theorem 2 and Theorem 3 we expect a spectral gap occurring between the $(2k+1)$ th and $(2k+2)$ th eigenvector of $H^{(k)}$ (counting multiplicities), and we choose aggregation (16) because the affinity measure (15) is related to the viewing angle by the relation (44) in Theorem 5. In particular, comparing (44) and [39, Theorem 6] tells us that

$$A_{ij}^{(k)} = A_{ij}^k \quad \text{for all } 1 \leq i \neq j \leq N.$$

We briefly sketch these results in the next subsection and defer more detailed discussions of this algorithm to Section 4.

Remark 1 Note that (15) and (16) are not the only ways to distill and aggregate the affinity information from multiple irreducible representations. Other natural alternatives include

$$G_{ij}^{(k)} := 2 \left(\frac{|\langle \Psi^{(k)}(I_i), \Psi^{(k)}(I_j) \rangle|}{\|\Psi^{(k)}(I_i)\| \|\Psi^{(k)}(I_j)\|} \right)^{\frac{1}{k}} - 1, \quad 1 \leq i \neq j \leq N \quad (17)$$

which in the noiseless scenario satisfies

$$G_{ij}^{(k)} = G_{ij}^{(1)} = 2A_{ij} - 1, \quad \text{for all } k \geq 1.$$

Therefore, it is natural to combing all $G_{ij}^{(k)}$ by arithmetic averaging

$$G_{ij}^{\text{All}} := \frac{1}{k_{\max}} \sum_{k=1}^{k_{\max}} G_{ij}^{(k)}. \quad (18)$$

However, our empirical experiments suggest that it is numerically much more stable to avoid taking k th roots for large values of k . We provide a brief interpretation of this phenomenon in Section 4.

1.2 Main Contributions

The main technical contribution of this paper is a complete characterization of the spectral information of a *generalized localized parallel transport operator* $T_h^{(k)}$, which is the continuous limit of the frequency- k class averaging matrix $H^{(k)}$ defined in (13), that involves general transport data $T^{(k)}(x, y)$ instead of $T(x, y)$ in (11). A formal definition for $T_h^{(k)}$ can be found in (33). We show in Theorem 2 and Theorem 3 that the top eigenspace of $T_h^{(k)}$, denoted as $\mathbb{W}^{(k)}$, is $(2k + 1)$ -dimensional, and the spectral gap grows as k increases. This fact alone speaks of the advantage of using higher frequency information for class averaging, as the *numerical stability* of the eigen-decomposition step in MFCA depends on the magnitude of the spectral gap.

In addition to the characterization of the dimensionality of the top eigenspace $\mathbb{W}^{(k)}$ of $T_h^{(k)}$, we also demonstrate in Theorem 4 and Theorem 5 the existence of a canonical identification of $\mathbb{W}^{(k)}$ with a complex $(2k + 1)$ -dimensional linear space spanned by $(2k + 1)$ linearly independent entry functions in the *Wigner D-matrix* associated with the unique $(2k + 1)$ -dimensional unitary irreducible representation of $\text{SO}(3)$. A direct corollary of this canonical identification is the equality between the frequency- k affinity measure (17) and the viewing angle, thus generalizing the result in [39] for the affinity measure (9). These facts establish the admissibility (consistency) of the proposed MFCA algorithm.

We emphasize that these theoretical results are not straightforward extensions of the techniques in [39] to the generalized localized parallel transport operator $T_h^{(k)}$. The generating-function-based approach in [39] is not easy to generalize to our setting without heavy notation and lengthy mathematical inductions. Instead, we observed that the constructions in [39] can be greatly simplified using an alternative construction by means of the Wigner D -matrices, which has been widely used in studies in mathematical physics concerning the unitary representation of $\text{SO}(3)$.

Besides the improved numerical stability due to increased spectral gap, using higher frequency information for class averaging can also be interpreted as leveraging the additional redundancy encoded in the consistency of the “higher order moments,” which is in line with our continued exploration for a “geometric harmonic retrieval” initiated in [34, 26, 27]. Moreover, in contrast with the computationally demanding SDP approach in [4] or the noise-type-dependent approximate message passing approach in [54], the proposed MFCA algorithm is easily parallelizable as the eigen-decompositions for the class averaging matrices in each frequency channel are completely independent.

1.3 Organization of the paper

The rest of this paper is organized as follows. Section 2 introduces the basic mathematical setup and recaptures properties of Wigner D - and d -matrices that are used in the remainder of this paper; Section 3 presents the main theoretical contributions; Section 4 interprets the admissibility and numerical stability of MFCA using the theoretical results; Section 5 illustrates the efficacy of MFCA through some numerical experiments; Section 6 concludes and discusses potential future directions. Technical proofs are deferred to Appendix A.

2 Preliminaries

2.1 Wigner’s D - and d -Matrices

In this section we briefly recall the definition and relevant properties of the Wigner’s D - and d -matrices, which will be used extensively in the rest of this paper for explicit computations related to the irreducible representations of $\text{SO}(3)$. Recall that elements of $\text{SO}(3)$ are realized as rotation matrices parametrized by *Euler angles* $(\varphi, \vartheta, \psi) \in [0, 2\pi) \times [0, \pi] \times [0, 2\psi)$: each $x \in \text{SO}(3)$ can be explicitly written as

$$x = x(\varphi, \vartheta, \psi) = \begin{pmatrix} \cos \varphi \cos \psi - \sin \varphi \sin \psi \cos \vartheta & -\cos \varphi \sin \psi - \sin \varphi \cos \psi \cos \vartheta & \sin \varphi \sin \vartheta \\ \sin \varphi \cos \psi + \cos \varphi \sin \psi \cos \vartheta & -\sin \varphi \sin \psi + \cos \varphi \cos \psi \cos \vartheta & -\cos \varphi \sin \vartheta \\ \sin \psi \sin \vartheta & \cos \psi \cos \vartheta & \cos \vartheta \end{pmatrix}. \quad (19)$$

Note that this is equivalent to writing $x = R_1(\varphi) R_2(\vartheta) R_3(\psi)$, where

$$R_1(\varphi) = \begin{pmatrix} 1 & 0 & 0 \\ 0 & \cos \varphi & -\sin \varphi \\ 0 & \sin \varphi & \cos \varphi \end{pmatrix}, \quad R_2(\vartheta) = \begin{pmatrix} \cos \vartheta & 0 & \sin \vartheta \\ 0 & 1 & 0 \\ -\sin \vartheta & 0 & \cos \vartheta \end{pmatrix}, \quad R_3(\psi) = \begin{pmatrix} \cos \psi & -\sin \psi & 0 \\ \sin \psi & \cos \psi & 0 \\ 0 & 0 & 1 \end{pmatrix}.$$

The last column in the matrix representation (19) is exactly the *view direction* corresponding to $x \in \text{SO}(3)$. For the simplicity of statements, we denote the viewing direction of $x \in \text{SO}(3)$ as

$$\pi(x) = \pi(x(\varphi, \vartheta, \psi)) = (\sin \varphi \sin \vartheta, -\cos \varphi \sin \vartheta, \cos \vartheta)^\top \in \mathbb{R}^3.$$

For each integer $\ell = 0, 1, 2, \dots$, the *Wigner's D-matrix* $\text{SO}(3) \ni x \mapsto D^\ell(x) \in \mathbb{C}^{(2\ell+1) \times (2\ell+1)}$ is the unique (up to isomorphism) irreducible matrix representation of $\text{SO}(3)$ of weight ℓ . For each $x \in \text{SO}(3)$, $D^\ell(x)$ is a $(2\ell+1)$ -by- $(2\ell+1)$ complex Hermitian matrix, of which the entries we denote by $D_{mn}^\ell(x)$ ($-\ell \leq m, n \leq \ell$). As group representations, we have for any $\ell = 0, 1, \dots$ and any $x, x' \in \text{SO}(3)$ the multiplicative formula

$$D^\ell(x') D^\ell(x) = D^\ell(x' \triangleright x) = D^\ell(x' \triangleright x). \quad (20)$$

The $2\ell+1$ entries in the central column of D^ℓ , i.e., D_{m0}^ℓ ($-\ell \leq m \leq \ell$), gives rise to the $2\ell+1$ independent spherical harmonics of degree ℓ . More generally, the $2\ell+1$ entries in the s th column ($-\ell \leq s \leq \ell$) of D^ℓ give rise to the $2\ell+1$ independent spin-weighted spherical harmonics of degree ℓ and weight s [21, 35]. Using the Euler angles, Wigner's D -matrices can be written explicitly as

$$D_{mn}^\ell(\varphi, \vartheta, \psi) := D_{mn}^\ell(x(\varphi, \vartheta, \psi)) = e^{-im\varphi} d_{mn}^\ell(\vartheta) e^{-in\psi}, \quad m, n = -\ell, \dots, \ell \quad (21)$$

where matrices $d^\ell(\varphi)$ are known as *Wigner's d-matrices*. They are real $(2\ell+1)$ -by- $(2\ell+1)$ matrices with an explicit formula for its (m, n) th entry as

$$d_{mn}^\ell(\vartheta) = (-1)^{\ell-n} [(\ell+m)! (\ell-m)! (\ell+n)! (\ell-n)!]^{1/2} \sum_s (-1)^s \frac{\left(\cos \frac{\vartheta}{2}\right)^{m+n+2s} \left(\sin \frac{\vartheta}{2}\right)^{2\ell-m-n-2s}}{s! (\ell-m-s)! (\ell-n-s)! (m+n+s)!}$$

with the sum running over all $s \in \mathbb{Z}$ that make sense of the factorials [50, §3.3.2]. We will only need the explicit form of d_{mn}^ℓ for the special case $m = n = -\ell$: In this case it is straightforward to verify that the summation consists of only one term $s = 2\ell$, and hence

$$d_{-\ell, -\ell}^\ell(\vartheta) = \left(\cos \frac{\vartheta}{2}\right)^{2\ell} = \left(\cos^2 \frac{\vartheta}{2}\right)^\ell = \left(\frac{1 + \cos \vartheta}{2}\right)^\ell. \quad (22)$$

Alternatively, d_{mn}^ℓ can also be written explicitly in terms of Jacobi polynomials as (see e.g. [50, §13.1.1])

$$d_{mn}^\ell(\vartheta) = 2^{-m} \left[\frac{(\ell-m)! (\ell+m)!}{(\ell-n)! (\ell+n)!} \right]^{\frac{1}{2}} (1 - \cos \vartheta)^{\frac{m-n}{2}} (1 + \cos \vartheta)^{\frac{m+n}{2}} P_{\ell-m}^{(m-n, m+n)}(\cos \vartheta) \quad (23)$$

where $\{P_n^{(a,b)} : n = 0, 1, 2, \dots\}$ denote the sequence of Jacobi polynomials with parameters a, b [50, §13.1.1]. This gives rise to the explicit formula for the diagonal entries of the Wigner d -matrices:

$$d_{mm}^\ell(\vartheta) = 2^{-m} (1 + \cos \vartheta)^m P_{\ell-m}^{(0, 2m)}(\cos \vartheta). \quad (24)$$

In particular, we see directly from (23) that

$$d_{mn}^\ell(0) = \delta_{mn} P_{\ell-m}^{(0, 2m)}(1) = \delta_{mn} \cdot \binom{\ell-m}{\ell-m} = \delta_{mn} \quad (25)$$

where δ_{mn} is the Kronecker delta notation

$$\delta_{mn} = \begin{cases} 1 & \text{if } m = n \\ 0 & \text{otherwise.} \end{cases}$$

If the Euler angles of x' take the form $(0, 0, \psi)$, then by (20) we have

$$D_{mn}^\ell((0, 0, \psi) \triangleright x) = \sum_{s=-\ell}^{\ell} D_{ms}^\ell(0, 0, \psi) D_{sn}^\ell(x) \stackrel{(21)}{=} \sum_{s=-\ell}^{\ell} d_{ms}^\ell(0) e^{-\iota s \psi} D_{sn}^\ell(x) \stackrel{(25)}{=} e^{-\iota m \psi} D_{mn}^\ell(x). \quad (26)$$

We will need this relation in the proof of Theorem 2.

Recall from [66, pp.21–22] that Euler angles admit physical interpretations for the rotation matrix: If we denote the canonical right-handed orthonormal basis in \mathbb{R}^3 by $\{\mathbf{e}_1, \mathbf{e}_2, \mathbf{e}_3\}$, and write $R_{\mathbf{e}_i}(\alpha) \in \text{SO}(3)$ for the rotation around axis \mathbf{e}_i ($i = 1, 2, 3$) by angle α , then rotation by $x(\varphi, \vartheta, \psi) \in \text{SO}(3)$ is equivalent to i) rotation by angle φ around \mathbf{e}_3 , ii) rotation by angle ϑ around the new axis $\mathbf{e}'_2 = R_{\mathbf{e}_3}(\varphi) \mathbf{e}_2$, and iii) rotation by angle ψ around the new axis $\mathbf{e}'_3 = R_{\mathbf{e}_3}(\varphi) R_{\mathbf{e}_2}(\vartheta) \mathbf{e}_3$. From this geometric interpretation, it is clear that the action of $\text{SO}(2)$ on $\text{SO}(3)$ considered throughout this paper only affects the Euler angle ψ . In other words, under the canonical identification of $\text{SO}(2)$ with $\text{SO}(3)$ elements of the form

$$h = h(\alpha) = \begin{pmatrix} \cos \alpha & -\sin \alpha & 0 \\ \sin \alpha & \cos \alpha & 0 \\ 0 & 0 & 1 \end{pmatrix}, \quad \alpha \in [0, 2\pi) \quad (27)$$

then $x(\varphi, \vartheta, \psi) \triangleleft h(\alpha) = x(\varphi, \vartheta, \psi + \alpha)$. Together with (21), this implies

$$\begin{aligned} D_{mn}^\ell(x(\varphi, \vartheta, \psi) \triangleleft h(\alpha)) &= D_{mn}^\ell(x(\varphi, \vartheta, \psi + \alpha)) \\ &= e^{-\iota n \alpha} D_{mn}^\ell(x(\varphi, \vartheta, \psi)) = \rho_n(h^{-1}) D_{mn}^\ell(x(\varphi, \vartheta, \psi)) \end{aligned} \quad (28)$$

where again ρ_n stands for the complex unitary irreducible representation of $\text{SO}(2)$ of character n .

2.2 Set-up

Throughout this paper, we view $\text{SO}(3)$ as a $\text{SO}(2)$ -bundle over the 2-dimensional sphere S^2 in \mathbb{R}^3 . For any $d \in \mathbb{N}_+$, we view \mathbb{C}^d as a Hilbert product space equipped with the canonical Hermitian inner product induced from the standard Euclidean inner product on \mathbb{R}^d . We will distinguish two different types of group actions on $\text{SO}(3)$: If $g \in \text{SO}(3)$, g acts on elements of $\text{SO}(3)$ by left multiplication, denoted as

$$g \triangleright g' := gg', \quad \forall g, g' \in \text{SO}(3).$$

If $h \in \text{SO}(2) \subset \text{SO}(3)$, unless otherwise specified, h is assumed to be identified with an $\text{SO}(3)$ element by (27) and acts on elements of $\text{SO}(3)$ by right multiplication, i.e.,

$$g' \triangleleft h := g'h, \quad \forall g' \in \text{SO}(3), h \in \text{SO}(2).$$

These actions induce corresponding actions on the linear space \mathcal{H} of complex-valued functions over \mathbb{C}^3 :

$$\begin{aligned} g \cdot f(x) &:= f(g^{-1} \triangleright x), \quad \forall f \in \mathcal{H}, x \in \text{SO}(3), g \in \text{SO}(3); \\ h \cdot f(x) &:= f(x \triangleleft h), \quad \forall f \in \mathcal{H}, x \in \text{SO}(3), h \in \text{SO}(2). \end{aligned}$$

Unless confusions arise, we will also denote $g' \triangleleft g =: g'g$, $g, g' \in \text{SO}(3)$ for the right action of $\text{SO}(3)$ on itself, when the context is clear.

3 Main Theoretical Results

3.1 Generalized Parallel Transport Operators

Let $\rho_k : \text{SO}(2) \rightarrow \mathbb{C}$ be the unique irreducible unitary representation of $\text{SO}(2)$ of character $k \in \mathbb{Z}$. Denote \mathcal{H} for the linear space of all complex-valued continuous functions on S^2 . Consider \mathcal{H} as a unitary representation of $\text{SO}(2)$, where $\text{SO}(2)$ acts on \mathcal{H} from the right by

$$h \cdot s(x) := s(x \triangleleft h), \quad \forall h \in \text{SO}(2), s \in \mathcal{H}, x \in S^2.$$

Denote the isotypic decomposition of this representation as

$$\mathcal{H} = \bigoplus_{k \in \mathbb{Z}} \mathcal{H}_k \tag{29}$$

where the action of $\text{SO}(2)$ on \mathcal{H}_k is given by

$$h \cdot s(x) = s(x \triangleleft h) = \rho_k(h) s(x), \quad \forall h \in \text{SO}(2), s \in \mathcal{H}_k, x \in S^2. \tag{30}$$

Note that $\text{SO}(3)$ acts on \mathcal{H}_k unitarily from the right by

$$g \cdot s(x) := s(g^{-1} \triangleright x), \quad \forall g \in \text{SO}(3), s \in \mathcal{H}_k, x \in S^2.$$

Each \mathcal{H}_k thus admits an isotypic decomposition with respect to $\text{SO}(3)$, written as

$$\mathcal{H}_k = \bigoplus_{n \in \mathbb{N}_{\geq 0}} \mathcal{H}_{n,k} \tag{31}$$

where $\mathcal{H}_{n,k}$ denotes the isotypic component corresponding to the unique irreducible representation of $\text{SO}(3)$ of dimension $(2n+1)$, for $n = 0, 1, \dots$. An important observation is that each $\mathcal{H}_{n,k}$ is of multiplicity 0 or 1 in \mathcal{H}_k :

Theorem 1 ([39, Theorem 7]) *If $n < |k|$ then $\mathcal{H}_{n,k} = 0$. Otherwise, $\mathcal{H}_{n,k}$ is isomorphic to the unique irreducible representation of $\text{SO}(3)$ of dimension $(2n+1)$.*

The motivation for considering these isotypic decompositions is to study the top eigenspace of the *generalized parallel transport operator* $T^{(k)} : \mathcal{H} \rightarrow \mathcal{H}$, defined as

$$\left(T^{(k)}s\right)(x) := \int_{S^2} \rho_k(T(x,y)) s(y) dy = \int_{S^2} T^{(k)}(x,y) s(y) dy, \quad \forall s \in \mathcal{H}, x \in S^2 \tag{32}$$

for all $k \in \mathbb{Z}$. When $k = 1$, $T^{(k)}$ reduces to the *parallel transport operator* $T : \mathcal{H} \rightarrow \mathcal{H}$ defined in [39, §2.3]. Similar to [39, §2.3.1], we can localize the generalized parallel transport operator $T^{(k)}$ for any $k \in \mathbb{Z}$ as

$$\left(T_h^{(k)}s\right)(x) := \int_{B(x,a)} \rho_k(T(x,y)) s(y) dy = \int_{B(x,a)} T^{(k)}(x,y) s(y) dy, \quad \forall s \in \mathcal{H}, x \in S^2 \tag{33}$$

where $B(x,a) = \{y \in S^2 \mid (\pi(x), \pi(y)) > \cos a =: 1 - h\}$ is a spherical cap on S^2 centered at $x \in S^2$. Using the symmetry, invariance, and equivariance of the transport data (Section 1.1.1), we establish the following basic properties of $T^{(k)}$ for any $k \in \mathbb{Z}$:

(1) $T^{(k)}$ is self-adjoint. This can be seen from the symmetry of transport data: for all $s, w \in \mathcal{H}$, we have

$$\begin{aligned} \left\langle T^{(k)}s, w \right\rangle_{\mathcal{H}} &= \int_{S^2} \int_{S^2} \rho_k(T(x,y)) s(y) \overline{w(x)} dy dx \\ &= \int_{S^2} \int_{S^2} s(y) \overline{\rho_k(T(y,x)) w(x)} dy dx = \left\langle s, T^{(k)}w \right\rangle_{\mathcal{H}}. \end{aligned}$$

- (2) $T^{(k)}$ commutes with the action of $\text{SO}(3)$ on \mathcal{H} : by the invariance of transport data we have for all $g \in \text{SO}(3)$ and $s \in \mathcal{H}$, $x \in S^2$

$$\begin{aligned} \left(T^{(k)}(g \cdot s)\right)(x) &= \int_{S^2} \rho_k(T(x, y)) s(g^{-1} \triangleright y) dy \stackrel{z:=g^{-1} \triangleright y}{=} \int_{S^2} \rho_k(T(g \triangleright (g^{-1} \triangleright x), g \triangleright z)) s(z) dz \\ &= \int_{S^2} \rho_k(T(g^{-1} \triangleright x, z)) s(z) dz = \left(T^{(k)}s\right)(g^{-1} \triangleright x) = \left(g \cdot \left(T^{(k)}s\right)\right)(x). \end{aligned}$$

- (3) $\bigoplus_{\ell \neq -k} \mathcal{H}_\ell \subset \ker T^{(k)}$, and $T^{(k)}$ can be viewed as an operator from \mathcal{H}_{-k} to itself. This can be verified using the equivariance of $T^{(k)}$. First, note that for any $s \in \mathcal{H}$ we have $T^{(k)}s \in \mathcal{H}_{-k}$, since for any $w \in \text{SO}(2)$ we have

$$\begin{aligned} w \cdot \left(T^{(k)}s\right)(x) &= \left(T^{(k)}s\right)(x \triangleleft w) \\ &= \int_{B(x,a)} \rho_k(T(x \triangleleft w, y)) s(y) dy = \int_{B(x,a)} \overline{\rho_k(w)} \rho_k(T(x, y)) s(y) dy \\ &= \rho_{-k}(w) \int_{B(x,a)} \rho_k(T(x, y)) s(y) dy = \rho_{-k}(w) \left(T^{(k)}s\right)(x). \end{aligned}$$

This proves that $T^{(k)}$ maps \mathcal{H} into \mathcal{H}_{-k} , by the definition of isotypic decomposition (30) with respect to the $\text{SO}(2)$ action. The conclusion that $\bigoplus_{\ell \neq -k} \mathcal{H}_\ell \subset \ker T^{(k)}$ then follows from Schur's Lemma [12, Theorem 2.1].

The arguments above can be applied to $T_h^{(k)}$, *mutatis mutandis*, and thus the same properties hold for the localized generalized parallel transport operator. Invoking Schur's Lemma for a second time, we know that $T_h^{(k)}$ acts on $\mathcal{H}_{n,-k}$ as a scalar, i.e.,

$$T_h^{(k)}|_{\mathcal{H}_{n,-k}} = \lambda_n^{(k)}(h) \text{Id}|_{\mathcal{H}_{n,-k}}. \quad (34)$$

The multiplicity-one theorem (Theorem 1) tells us that $\lambda_n^{(k)} = 0$ for all $0 \leq n < |k|$. In order to calculate the remaining $\lambda_n^{(k)}$'s ($n \geq |k|$) explicitly, it suffices to fix a point $x_0 \in \text{SO}(x)$, and pick an arbitrary function $u \in \mathcal{H}_{n,-k}$ with $u(x_0)$, and use relation $\lambda_n^{(k)} = \left(T_h^{(k)}u\right)(x_0)/u(x_0)$. We will defer such computations for $0 < h \ll 1$ to Section 3.2. Next subsection summarizes these properties, in preparation for the discussion on the main algebraic structure of the *generalized intrinsic model* in Section 3.3.

3.2 Spectral Properties of the Localized Parallel Transport Operator

In this subsection we summarize the spectral properties of $T_h^{(k)}$ for $h \ll 1$ (which is the relevant regime for class averaging). Proofs for all the results discussed in this subsection are deferred to Appendix A; these proofs essentially follow the proofs of [39, Theorem 3 and Theorem 4], with slight technical modification due to the complication of Jacobi polynomials — unlike the case for the Legendre polynomials involved in the analysis of single-frequency class averaging, no sharp Bernstein-type inequality is known for Jacobi polynomials arising from the Wigner d -matrices. We refer interested readers to discussions and conjectures in [15, 37, 45] for Bernstein-type inequalities for Jacobi polynomials.

Theorem 2 (Eigenvalues of $T_h^{(k)}$ for small $h \ll 1$) *The operator $T_h^{(k)}$ has a discrete spectrum $\lambda_n^k(h)$ for all $n \in \mathbb{N}$, and $\lambda_n^{(k)} = 0$ for all $0 \leq n < |k|$. For $n \geq |k|$ and $h \in (0, 2]$, the dimension of the eigenspace of $T_h^{(k)}$ corresponding to $\lambda_n^{(k)}$ is $2n + 1$. More precisely, in the regime $h \ll 1$, the eigenvalue $\lambda_n^{(k)}(h)$ ($n \geq |k|$) adopts asymptotic expansion*

$$\lambda_n^{(k)}(h) = \frac{1}{2}h - \frac{1}{8}(n^2 + n - k^2) + O(h^3). \quad (35)$$

Remark 2 When $k = 1$, Theorem 2 reduces to [39, Theorem 3].

The proof of Theorem 2 in Appendix A.1 actually proves the stronger conclusion that each eigenvalue $\lambda_n^{(k)}(h)$ is a polynomial in $h > 0$ of degree $(n + 1)$ whenever $n \geq |k|$. The largest three eigenvalues for cases $k = 1$ and $k = 2$ can be explicitly written out as

$$\begin{aligned}\lambda_1^{(1)}(h) &= \frac{1}{2}h - \frac{1}{8}h^2, \\ \lambda_2^{(1)}(h) &= \frac{1}{2}h - \frac{5}{8}h^2 + \frac{1}{6}h^3, \\ \lambda_3^{(1)}(h) &= \frac{1}{2}h - \frac{11}{8}h^2 + \frac{25}{24}h^3 - \frac{15}{64}h^4,\end{aligned}\tag{36}$$

and

$$\begin{aligned}\lambda_2^{(2)}(h) &= \frac{1}{2}h - \frac{1}{4}h^2 + \frac{1}{24}h^3, \\ \lambda_3^{(2)}(h) &= \frac{1}{2}h - h^2 + \frac{13}{24}h^3 - \frac{3}{32}h^4, \\ \lambda_4^{(2)}(h) &= \frac{1}{2}h - 2h^2 + \frac{57}{24}h^3 - \frac{70}{64}h^4 + \frac{7}{40}h^5.\end{aligned}\tag{37}$$

Plots of $\lambda_{k+i}^{(k)}$, for $i = 0, 1, 2$ are provided in Fig. 1. It is natural to conjecture that the top eigenspace of $T_h^{(k)}$ is the $(2k + 1)$ -dimensional space corresponding to eigenvalue $\lambda_k^{(k)}(h)$ for sufficiently small $h > 0$. Moreover, denote

$$\Delta_k := \arg \max_{h \in (0, 2]} \lambda_{k+1}^{(k)}(h) = \frac{1}{k+1},$$

we have the following characterization of the *spectral gap* for $T_h^{(k)}$ in the regime $0 < h \ll 1$.

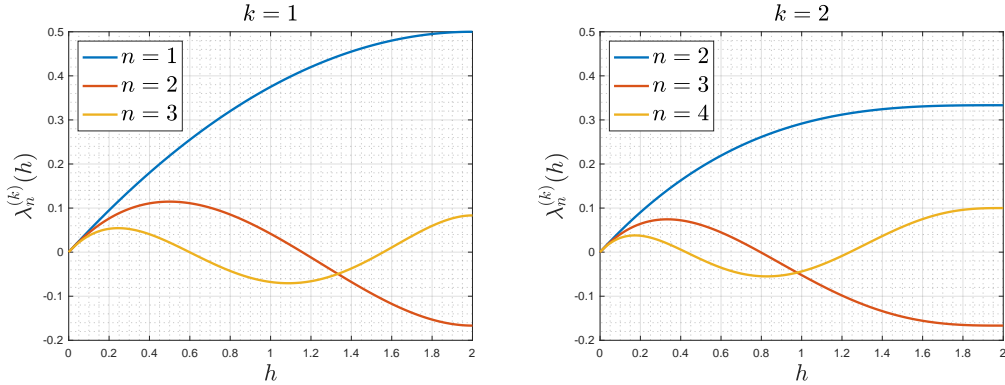


Fig. 1: The top three eigenvalues $\lambda_n^{(k)}(h)$ of operator $T_h^{(k)}$, for $k = 1$ (left) and $k = 2$ (right) over interval $h \in (0, 2]$.

Theorem 3 For every value of $h \in (0, 2]$, the largest eigenvalue of $T_h^{(k)}$ is $\lambda_k^{(k)}(h)$. In addition, for every value of $h \in (0, \Delta_k]$, the spectral gap $G^{(k)}(h)$ between the largest and the second largest eigenvalue of $T_h^{(k)}$ is

$$G^{(k)}(h) = \frac{2^{k+2} - (2-h)^{k+1}((k+1)h+2)}{2^{k+1}(k+2)}.\tag{38}$$

Again, when $k = 1$, Theorem 3 reduces to [39, Theorem 4]. For small $0 < h \ll 1$, the spectral gap is approximately

$$G^{(k)}(h) \sim \frac{1+k}{4}h^2\tag{39}$$

which gets larger as the “angular frequency” $k \in \mathbb{N}$ increases. This justifies one benefit of setting $k > 1$ for class averaging, as larger spectral gaps provide more robustness to noise corruption. The main technicality of the proof of Theorem 3, which is deferred to Appendix A.2, is to show that $\lambda_n^{(k)}(h) \leq \lambda_2(h)$ for every $h \in (0, \Delta_k]$, which appears evident from Figure 1.

3.3 The Main Algebraic Structure: Generalized Intrinsic Model

Just as the intrinsic model established in [39] equates the “extrinsic model” S^2 with the “intrinsic model” of the top eigenspace \mathbb{W} of $T = T^{(1)}$, we will generalize this correspondence to the setting for general complex irreducible unitary representations of $\text{SO}(2)$. More specifically, we establish the correspondence between the following two generalized models:

- *Generalized Extrinsic Model*: For every point $x = x(\varphi, \vartheta, \psi) \in \text{SO}(3)$, denote by $\delta_x^{(k)} : \mathbb{C} \rightarrow \mathbb{C}^{2k+1}$ for the unique complex morphism sending $1 \in \mathbb{C}$ to the first (index- $(-k)$) column of the Wigner D -matrix D^k , i.e.,

$$D_{\cdot, -k}^k(x) = (D_{-k, -k}^k(x), D_{-k+1, -k}^k(x), D_{-k+2, -k}^k(x), \dots, D_{k-1, -k}^k(x), D_{k, -k}^k(x))^{\top} \in \mathbb{C}^{2k+1}.$$

- *Generalized Intrinsic Model*: Define $\mathbb{W}^{(k)}$ as the top eigenspace of $T_h^{(k)}$, which by Theorem 2 and 3, is $(2k+1)$ -dimensional. Set for every point $x \in \text{SO}(3)$ the map

$$\varphi_x^{(k)} = \sqrt{1/(2k+1)} \cdot (\text{ev}_x | \mathbb{W}^{(k)})^* : \mathbb{C} \rightarrow \mathbb{W}^{(k)}, \quad (40)$$

where $\text{ev}_x : \mathcal{H} \rightarrow \mathbb{C}$ is the evaluation morphism at the point $x \in \text{SO}(3)$.

The main algebraic structure of the multi-frequency intrinsic classification algorithm is summarized in the following main theorem of this section.

Theorem 4 *The morphism $\tau : \mathbb{C}^{2k+1} \rightarrow \mathcal{H}$ defined by*

$$\begin{aligned} \tau : \mathbb{C}^{2k+1} &\longrightarrow \mathcal{H} \\ v &\longmapsto \left(x \mapsto \sqrt{2k+1} \cdot \left(\delta_x^{(k)} \right)^* (v) \right) \end{aligned}$$

is an isomorphism between \mathbb{C}^{2k+1} and $\mathbb{W}^{(k)} \subset \mathcal{H}$ (as Hermitian vector spaces). Moreover, for every $x \in \text{SO}(3)$ and $k = 0, 1, \dots$ there holds

$$\tau \circ \delta_x^{(k)} = \varphi_x^{(k)}. \quad (41)$$

Proof (Proof of Theorem 4) Our proof extends the arguments in the proof of [39, Theorem 5]. A key observation is that the top eigenvector $\mathcal{H}(\lambda_{\max}^{(k)}(h))$ coincides with the isotypic subspace $\mathcal{H}_{k, -k}$ (see Section 3.1). Consider the morphism $\alpha := \sqrt{1/(2k+1)} \cdot \tau : \mathbb{C}^{2k+1} \rightarrow \mathcal{H}$ defined as

$$\alpha(v)(x) = \left(\delta_x^{(k)} \right)^* (v).$$

Part 1: τ is an isomorphism between \mathbb{C}^{2k+1} and $\mathcal{H}_{k, -k}$. We first show that $\text{Im}(\alpha) \subset \mathcal{H}_{k, -k}$, namely, for any $x \in \text{SO}(3)$, $v \in \mathbb{C}^{2k+1}$, and $g \in \text{SO}(2)$ there holds

$$\left(\delta_{x \triangleleft g}^{(k)} \right)^* (v) = \rho_k(g^{-1}) \left(\delta_x^{(k)} \right)^* (v). \quad (42)$$

To this end, note that for any $z \in \mathbb{C}$ we have

$$\begin{aligned} \left\langle \left(\delta_{x \triangleleft g}^{(k)} \right)^* (v), z \right\rangle_{\mathbb{C}} &= \left\langle v, \delta_{x \triangleleft g}^{(k)}(z) \right\rangle_{\mathbb{C}^3} = \left\langle v, z D_{\cdot, -k}^k(x \triangleleft g) \right\rangle_{\mathbb{C}^3} \\ &\stackrel{(28)}{=} \left\langle v, z \rho_{-k}(g^{-1}) D_{\cdot, -k}^k(x) \right\rangle_{\mathbb{C}^3} = \left\langle v, z \rho_k(g) D_{\cdot, -k}^k(x) \right\rangle_{\mathbb{C}^3} = \left\langle \rho_k(g^{-1}) v, z D_{\cdot, -k}^k(x) \right\rangle_{\mathbb{C}^3} \\ &= \left\langle \rho_k(g^{-1}) v, \delta_x^{(k)}(z) \right\rangle_{\mathbb{C}^3} = \left\langle \rho_k(g^{-1}) \left(\delta_x^{(k)} \right)^* (v), z \right\rangle_{\mathbb{C}^3} \end{aligned}$$

which proves (42). Next, we show that α is a morphism of $\text{SO}(3)$ representations, namely, for any $x \in \text{SO}(3)$, $v \in \mathbb{C}^{2k+1}$, and $g \in \text{SO}(3)$ there holds

$$\left(\delta_x^{(k)} \right)^* (D^k(g)v) = \left(\delta_{g^{-1} \triangleright x}^{(k)} \right)^* (v). \quad (43)$$

To this end, again for any arbitrary $z \in \mathbb{C}$

$$\begin{aligned} \left\langle \left(\delta_x^{(k)} \right)^* \left(D^k(g)v \right), z \right\rangle_{\mathbb{C}} &= \left\langle D^k(g)v, \delta_x^{(k)}(z) \right\rangle_{\mathbb{C}^3} = \left\langle D^k(g)v, z D_{\cdot, -k}^k(x) \right\rangle_{\mathbb{C}^3} = \left\langle v, z D^k(g^{-1}) D_{\cdot, -k}^k(x) \right\rangle_{\mathbb{C}^3} \\ &\stackrel{(20)}{=} \left\langle v, z D_{\cdot, -k}^k(g^{-1} \triangleright x) \right\rangle_{\mathbb{C}^3} = \left\langle v, \delta_{g^{-1} \triangleright x}^{(k)}(z) \right\rangle_{\mathbb{C}^3} = \left\langle \left(\delta_{g^{-1} \triangleright x}^{(k)} \right)^* (v), z \right\rangle_{\mathbb{C}} \end{aligned}$$

which proves (43). It now follows immediately that the morphism α maps \mathbb{C}^{2k+1} isomorphically, as a unitary representation of $\text{SO}(3)$, onto $\mathcal{H}_{k, -k}$, the unique isotypical component in \mathcal{H}_{-k} (by (42)) of unitary irreducible $\text{SO}(3)$ -representation of dimension $2k+1$. This in turn implies that α (and thus τ) is an isomorphism between Hermitian vector spaces. It remains to determine the suitable normalization constant; we show that $\text{Tr}(\tau^* \circ \tau) = 2k+1$. Indeed,

$$\begin{aligned} \text{Tr}(\tau^* \circ \tau) &= (2k+1) \text{Tr}(\alpha^* \circ \alpha) = (2k+1) \int_{\mathbb{C}S^{2k}} \langle \alpha^* \circ \alpha(v), v \rangle_{\mathcal{H}} dv = (2k+1) \int_{\mathbb{C}S^{2k}} \langle \alpha(v), \alpha(v) \rangle_{\mathcal{H}} dv \\ &= (2k+1) \int_{\mathbb{C}S^{2k}} \int_{\text{SO}(3)} \left\langle \left(\delta_x^{(k)} \right)^* (v), \left(\delta_x^{(k)} \right)^* (v) \right\rangle_{\mathbb{C}} dx dv \\ &= (2k+1) \int_{\mathbb{C}S^{2k}} \int_{\text{SO}(3)} \left\langle \left(D_{\cdot, -k}^k(x) \right)^* v, \left(D_{\cdot, -k}^k(x) \right)^* v \right\rangle_{\mathbb{C}} dx dv \\ &= (2k+1) \int_{\mathbb{C}S^{2k}} \int_{\text{SO}(3)} 1 dx dv = 2k+1 \end{aligned}$$

where $\mathbb{C}S^{2k}$ is the $(4k+1)$ -dimensional unit sphere in \mathbb{C}^{2k+1} , and dv is the unique normalized Haar measure on $\mathbb{C}S^{2k}$.

Part 2: Proof of (41). By (42) we have $(\text{ev}_x | \mathbb{W}^{(k)}) \circ \alpha = \left(\delta_x^{(k)} \right)^*$, which is equivalent to $\left(\varphi_x^{(k)} \right)^* \circ \tau = \left(\delta_x^{(k)} \right)^*$. The conclusion now follows from the straightforward computation as in the proof of [39, Theorem 5]:

$$\left(\varphi_x^{(k)} \right)^* \circ \tau = \left(\delta_x^{(k)} \right)^* \Rightarrow \left(\varphi_x^{(k)} \right)^* \circ (\tau \circ \tau^*) = \left(\delta_x^{(k)} \right)^* \circ \tau^* \Rightarrow \left(\varphi_x^{(k)} \right)^* = \left(\delta_x^{(k)} \right)^* \circ \tau^* \Rightarrow \tau \circ \delta_x^{(k)} = \varphi_x^{(k)}.$$

This completes the entire proof. \square

Furthermore, Theorem 4 reveals the correspondence between the generalized extrinsic and intrinsic models, in terms of the viewing angle information they encode. This is summarized in the following result.

Theorem 5 *For every pair of frames $x, y \in \text{SO}(3)$, we have*

$$\left| \langle \varphi_x^{(k)}(v), \varphi_y^{(k)}(u) \rangle_{\mathbb{W}^{(k)}} \right| = \left(\frac{\langle \pi(x), \pi(y) \rangle + 1}{2} \right)^k \quad (44)$$

for any choice of unit-norm complex numbers $v, u \in \mathbb{C}$.

Proof (Proof of Theorem 5) By Theorem 4, τ is a morphism between Hermitian inner product spaces \mathbb{C}^{2k+1} and $\mathbb{W}^{(k)}$ and (41) holds, thus by the same argument in the last step of the proof of [39, Theorem 6] it suffices to prove that for any unit-norm complex numbers $v, u \in \mathbb{C}$ there holds

$$\left| \left\langle \delta_x^{(k)}(u), \delta_y^{(k)}(v) \right\rangle_{\mathbb{C}^{2k+1}} \right| = \left(\frac{\langle \pi(x), \pi(y) \rangle + 1}{2} \right)^k. \quad (45)$$

This boils down to the following straightforward computation:

$$\begin{aligned} \left| \left\langle \delta_x^{(k)}(u), \delta_y^{(k)}(v) \right\rangle_{\mathbb{C}^{2k+1}} \right| &= \left| u \left(D_{\cdot, -k}^k(x) \right)^\top \left(D_{\cdot, -k}^k(y) \right)^* \bar{v} \right| = \left| D_{-k, -k}^k(x^{-1}y) \right| \\ &\stackrel{(21)}{=} \left| d_{-k, -k}^k(\vartheta(x^{-1}y)) \right| \stackrel{(22)}{=} \left(\frac{1 + \cos \vartheta(x^{-1}y)}{2} \right)^k \end{aligned} \quad (46)$$

where $\vartheta(x^{-1}y)$ is the Euler angle ϑ of $x^{-1}y \in \text{SO}(3)$. Recall from (19) that $\cos \vartheta(x^{-1}y)$ is exactly the $(3, 3)$ -entry of the 3-by-3 matrix form of $x^{-1}y \in \text{SO}(3)$, which is exactly identical to the inner product of the third columns of the matrix forms of x and y , i.e.,

$$\cos \vartheta(x^{-1}y) = \langle \pi(x), \pi(y) \rangle.$$

Plugging this back into the rightmost term of (46) completes the entire proof. \square

Remark 3 When $k = 1$, Theorem 4 and Theorem 5 reduce to [39, Theorem 5] and [39, Theorem 6], respectively, up to a different scaling constant for τ . The difference arises from our alternative, explicit construction of the isomorphism τ using Wigner D -matrices.

4 Interpretation of the Theoretical Results for Multi-Frequency Class Averaging

In this section, we interpret the MFCA algorithm stated in Section 1.1.2 using the theoretical results established in Section 3, and provide conceptual explanations for the admissibility and stability of MFCA.

First, under the assumption that the projection images $\{I_i \mid 1 \leq i \leq N\}$ are produced from orthonormal frames $\{x_i \mid 1 \leq i \leq N\}$ sampled i.i.d. uniformly on $\text{SO}(3)$ with respect to the normalized Haar measure, we know from standard results [44, Theorem 3.1] that the eigenvalues of $H^{(k)}$, the class averaging matrix at frequency k defined in Section 1.1.2, converges to the eigenvalues of the generalized localized parallel transport operator $T_h^{(k)}$ defined in (33) as the number of samples N goes to infinity, provided that the bandwidth parameter h lies in a sufficiently small regime. In particular, this implies that for large sample size N the spectral gap of (a properly rescaled version of) $H^{(k)}$ converges to the spectral gap of $T_h^{(k)}$, which, by Theorem 2 and Theorem 3, is roughly of size $(1+k)h^2/4$ and occurs between the $(2k+1)$ th and the $(2k+2)$ th eigenvalues of $H^{(k)}$ (ranked in decreasing order). Noticeably, the spectral gap gets larger for higher frequency index k , which implies that the linear space spanned by the first $(2k+1)$ eigenvectors of $H^{(k)}$ is closer to the top eigenspace of $T_h^{(k)}$, since the approximation error is inversely proportional to the spectral gap according to the renowned Davis–Kahan theorem [18, 69]. This also explains the choice of extracting the top $(2k+1)$ eigenvectors of $H^{(k)}$ in MFCA.

Moreover, as argued in [39, Theorem 2], the MFCA embedding $\Psi^{(k)}$ defined in (14) corresponds to the morphism (40) in the following form:

$$\frac{\Psi^{(k)}(x_i)}{\|\Psi^{(k)}(x_i)\|} = \varphi_{x_i}^{(k)}(1), \quad \text{for all } x_i \in \text{SO}(3)$$

where $\|\cdot\|$ stands for the standard norm on \mathbb{C}^{2k+1} . Using results from ℓ_∞ -norm eigenvector perturbation analysis [24, 1, 25, 72], we know from Theorem 5 that the absolute value of the correlation between $\Psi^{(k)}(I_i)$ and $\Psi^{(k)}(I_j)$ is close to

$$\left| \left\langle \varphi_{x_i}^{(k)}(1), \varphi_{x_j}^{(k)}(1) \right\rangle \right| = \left(\frac{\langle \pi(x_i), \pi(x_j) \rangle + 1}{2} \right)^k$$

which provides justification for the admissibility of the MFCA algorithm. In fact, Theorem 5 tells us that the affinity measure $G_{ij}^{(k)}$ defined in (17) coincides precisely with the cosine value for the angle between the two viewing directions in the noiseless regime. As k increases, the spectral gap of $H^{(k)}$ also increases, which by the ℓ_∞ -norm perturbation analysis of eigenvectors (see e.g. [1, Theorem 2.1]) implies the increased accuracy of the approximation

$$A_{ij}^{(k)} = \frac{|\langle \Psi^{(k)}(I_i), \Psi^{(k)}(I_j) \rangle|}{\|\Psi^{(k)}(I_i)\| \|\Psi^{(k)}(I_j)\|} \approx \left(\frac{\langle \pi(x_i), \pi(x_j) \rangle + 1}{2} \right)^k \quad (47)$$

since the ℓ_∞ -norm perturbation error of the eigenvectors is bounded inverse-proportionally with respect to the spectral gap. The form of the approximation identity (47) also suggests avoiding directly taking the k th root of the correlation between $\Psi^{(k)}(I_i)$ and $\Psi^{(k)}(I_j)$ as in (17) and (18) since this approach loses control of the numerical relative error. In contrast, it is advantageous to use the multiplicative forms (15) and (16) which do not worsen the relative error. One may well expect other linear combinations of the $A_{ij}^{(k)}$'s, which are degree- k_{\max} polynomials of the (cosine value of the) viewing angle, will make small viewing angles much more prominent in the numerical procedures; we leave these further explorations to future work.

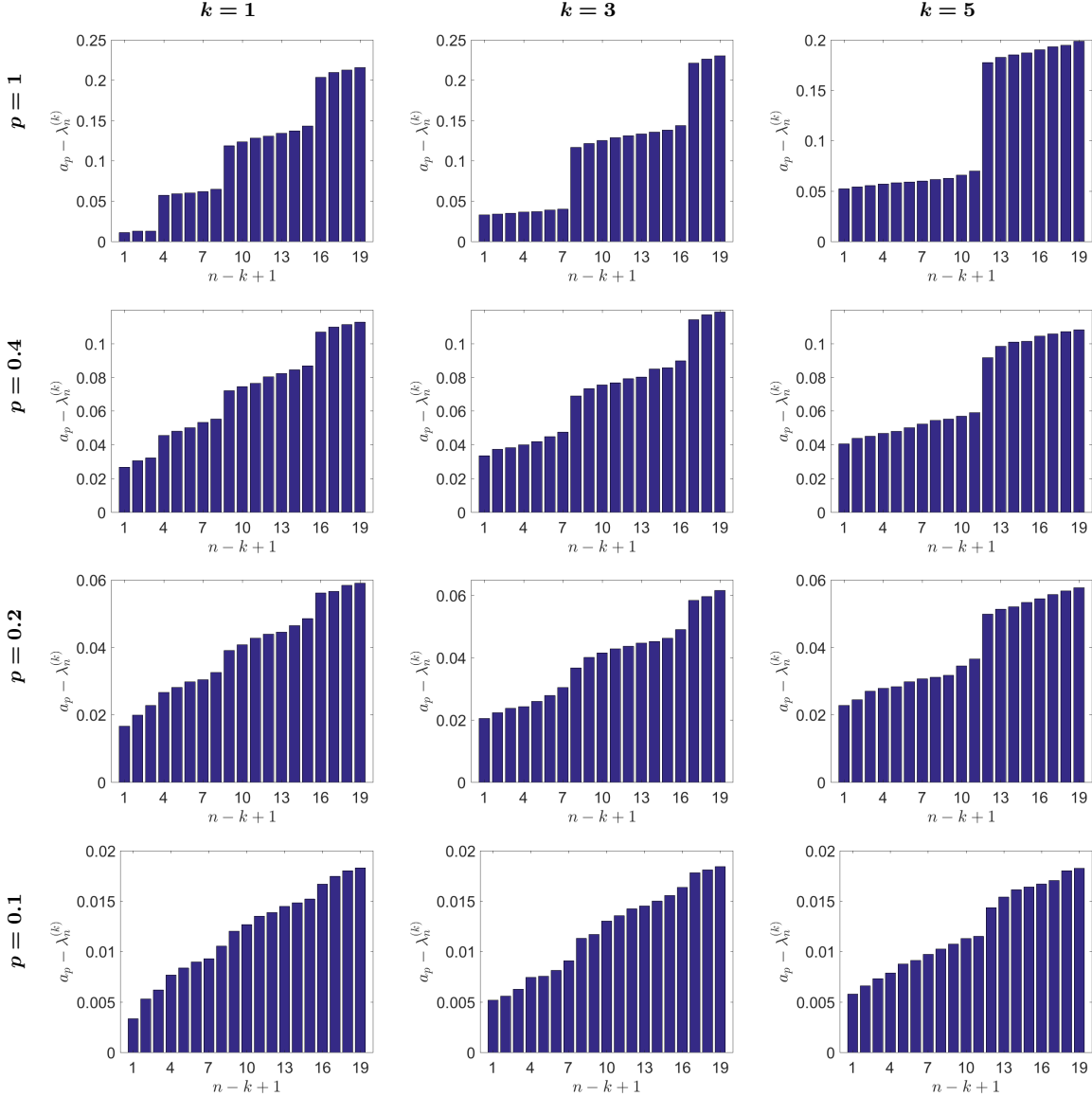


Fig. 2: Bar plots of the 19 largest eigenvalues $\{\lambda_n^{(k)}\}_{n-k=0}^{19}$ of the $\tilde{H}^{(k)}$ at different k and p values. To better illustrate the spectral gaps, the y -axis corresponds to $a_p - \lambda$, with $a_1 = 1$, $a_{0.4} = 0.45$, $a_{0.2} = 0.25$, and $a_{0.1} = 0.15$.

5 Numerical Results

We conducted two sets of numerical experiments. The first set involves simulations of the probabilistic model introduced in [63]. The second set applies the proposed algorithm on the noisy simulated projection images of a 3-D volume of 70S ribosome. We point out that there is no direct way to compare the performance of classification algorithms on real microscope images, since their viewing directions are unknown. The only way to compare classification algorithms on real data is indirectly, by evaluating the resulting 3-D reconstructions. Here we conduct only numerical experiments from which conclusions can be drawn directly for 2-D images. All experiments in this section were executed on a Linux machine with 16 Intel Xeon 2.5GHz cores and 512GB of RAM.

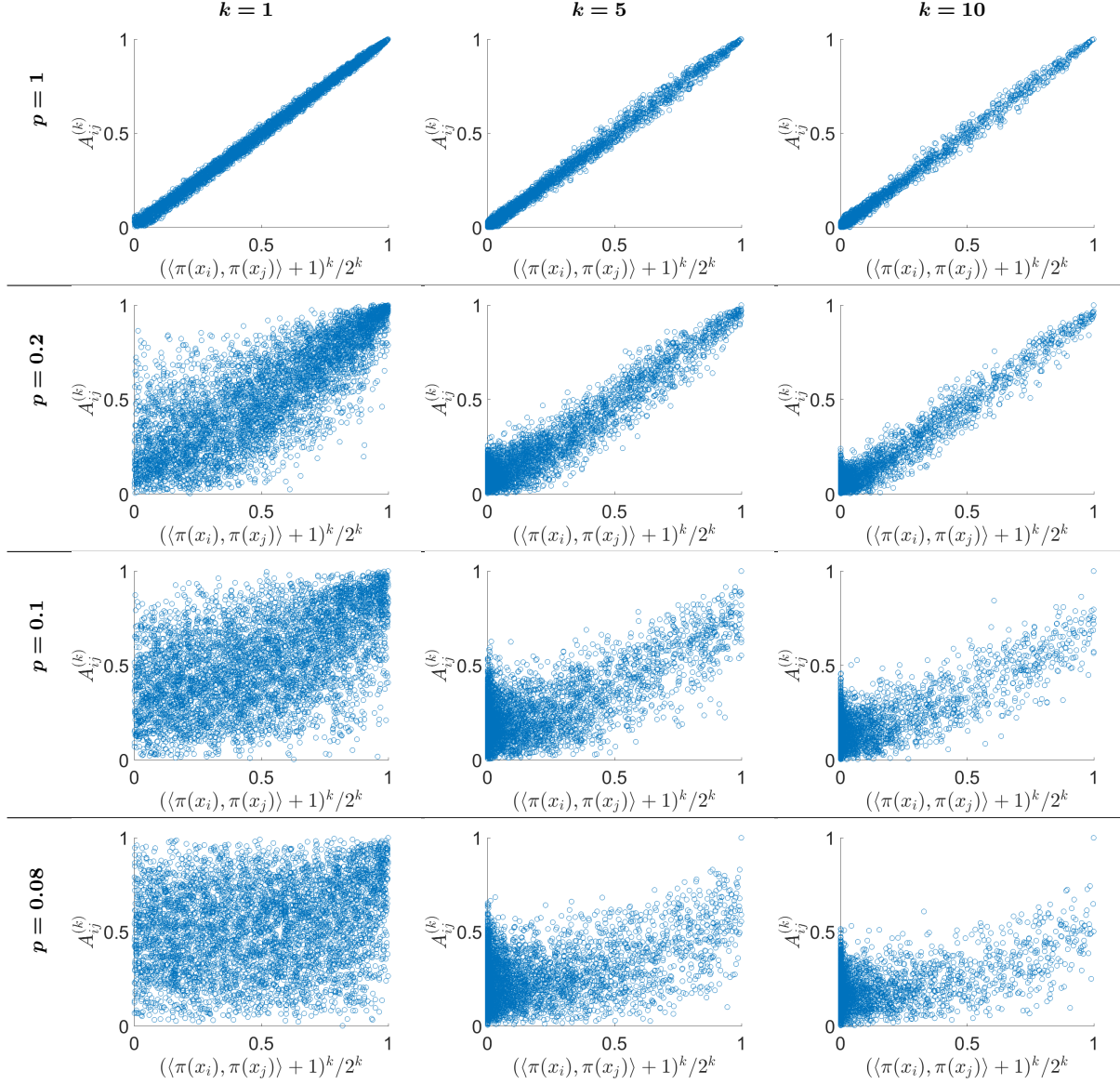


Fig. 3: Scatter plots of $A_{ij}^{(k)}$ against $(\langle \pi(x_i), \pi(x_j) \rangle + 1)^k / 2^k$ at $p = 1, 0.2, 0.1$ and 0.08 and $k = 1, 5,$ and 10 . The robustness of the approximation (47) is considerably more robust for larger values of k .

5.1 Experiments with Probabilistic Models

We first generate $N = 10,000$ orthonormal frames x_1, \dots, x_N in \mathbb{R}^3 , uniformly sampled from $\text{SO}(3)$ with respect to the normalized Haar measure. Each frame x_i can be represented by a 3×3 orthogonal matrix $R_i = [R_i^1, R_i^2, R_i^3]$ and $\det(R_i) = 1$. We identify the third column R_i^3 as the *viewing angle* $\pi(x_i)$ of the molecule. The clean geometric neighborhood graph is constructed by connecting points where $\langle \pi(x_i), \pi(x_j) \rangle > 0.95$ (within 19.2° opening angle). The first two columns R_i^1 and R_i^2 form an orthonormal basis for the plane in \mathbb{R}^3 perpendicular to the viewing angle $\pi(x_i)$. If x_i and x_j are two rotations with the same viewing angle, $\pi(x_i) = \pi(x_j)$, then R_i^1, R_i^2 and R_j^1, R_j^2 are two orthogonal bases for the same plane and the rotation matrix $R_i^{-1}R_j$ has the following form:

$$R_i^{-1}R_j = \begin{pmatrix} \cos \theta_{ij} & -\sin \theta_{ij} & 0 \\ \sin \theta_{ij} & \cos \theta_{ij} & 0 \\ 0 & 0 & 1 \end{pmatrix}. \quad (48)$$

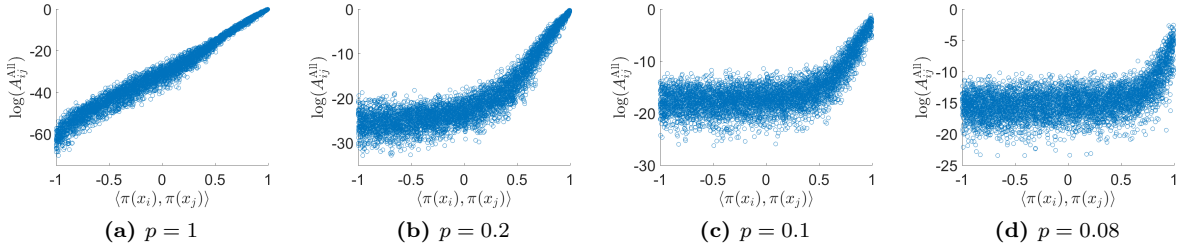


Fig. 4: Scatter plots for log multi-frequency class averaging affinity $\log A_{ij}^{\text{all}}$ against $\langle \pi(x_i), \pi(x_j) \rangle$ at $p = 1, 0.2, 0.1$ and 0.08 .

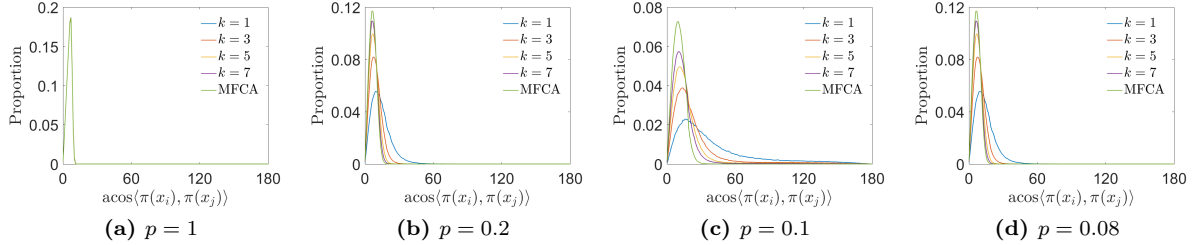


Fig. 5: Histogram of the angles (x -axis, in degrees) between the viewing directions of 10,000 simulated frames and its 50 neighboring points at $p = 1, 0.2, 0.1, 0.08$.

When the viewing angles are slightly different, (48) holds approximately. The optimal in-plane rotational angle θ_{ij} provides a good approximation to the angle $\tilde{\theta}_{ij}$ that “aligns” the orthonormal bases for the planes $\pi(x_i)^\perp$ and $\pi(x_j)^\perp$. Therefore, if $\langle \pi(x_i), \pi(x_j) \rangle$ is close to 1, the angle θ_{ij} approximates the $\tilde{\theta}_{ij}$ given by

$$\tilde{\theta}_{ij} = \arg \min_{\theta \in [0, 2\pi)} \|R_i \rho(\theta) - R_j\|_F, \quad \text{with } \rho(\theta) = \begin{pmatrix} \cos \theta & -\sin \theta & 0 \\ \sin \theta & \cos \theta & 0 \\ 0 & 0 & 1 \end{pmatrix}. \quad (49)$$

In other words, the ground truth local parallel transport data is computed by aligning the local frames within the connected neighborhood, determined by the entries of the matrix $R_i^{-1}R_j$:

$$\begin{aligned} \cos \tilde{\theta}_{ij} &= \frac{(R_i^{-1}R_j)_{11} + (R_i^{-1}R_j)_{22}}{\sqrt{[(R_i^{-1}R_j)_{11} + (R_i^{-1}R_j)_{22}]^2 + [(R_i^{-1}R_j)_{21} - (R_i^{-1}R_j)_{12}]^2}}, \\ \sin \tilde{\theta}_{ij} &= \frac{(R_i^{-1}R_j)_{21} - (R_i^{-1}R_j)_{12}}{\sqrt{[(R_i^{-1}R_j)_{11} + (R_i^{-1}R_j)_{22}]^2 + [(R_i^{-1}R_j)_{21} - (R_i^{-1}R_j)_{12}]^2}}. \end{aligned} \quad (50)$$

To generate the noisy graph under the probabilistic model introduced in [63], we keep the correct edge in the neighborhood graph with probability p , and use the ground truth local parallel transport data $e^{ik\tilde{\theta}_{ij}}$ in (50). With probability $1 - p$, we rewired the edge such that the node i is connected to a randomly selected node that is not connected with i . For the rewired edge, the optimal in-plane rotational alignment angle is replaced with an angle uniformly sampled from 0 to 2π . We compute the the eigenvalues and eigenvectors of the normalized Hermitian matrix, $\tilde{H}^{(k)} = D^{-1/2}HD^{-1/2}$.

Fig. 2 shows the spectral properties of the top eigenvalues of $\tilde{H}^{(k)}$ according to Theorem 2. The multiplicities $2k + 1, 2k + 3, 2k + 5, \dots$ of the top eigenvalues are clearly demonstrated in the bar plots for $p = 1$ (the first row in Fig. 2). As p decreases, the top spectral gap gets smaller and when $p = 0.1$, it is hard to identify the spectral gap for $k = 1$, whereas the top spectral gap at $k = 5$ is still noticeable. This is consistent with our expectation for improved spectral stability for larger k .

The estimated $A_{ij}^{(k)}$'s provide good approximations to $(\langle \pi(x_i), \pi(x_j) \rangle + 1)^k / 2^k$ (see the top row of Fig. 3). This approximation deteriorates as p decreases. The lower left sub-figure of Fig. 3 shows that the original

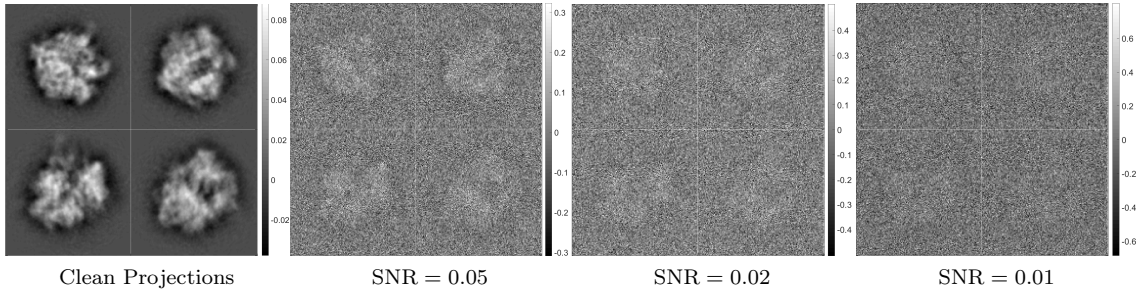


Fig. 6: Samples of simulated projection images on 70S ribosome. From *left to right*: Clean projection images, images contaminated by additive white Gaussian noise with signal to noise ratio SNR = 0.05, 0.02, 0.01.

single frequency class averaging nearest neighbor search algorithm fails at $p = 0.08$. Fig. 4 shows the scatter plots of the combined affinity against the dot products $\langle \pi(x_i), \pi(x_j) \rangle$ between the true viewing angles at varying p . Even at $p = 0.08$, the combined affinity A_{ij}^{All} is still able to identify frames of similar viewing directions, in contrast to the approximation results in Fig. 3.

We evaluate the performance of the proposed algorithms on the nearest neighbor search by inspecting the magnitudes of the angles between the viewing directions of frames identified as neighbors by the algorithm. We identify for each frame 50 nearest neighbors with respect to the affinity measure, and plot in Fig. 5 the histogram of the angles between the viewing directions of neighboring frames for varying rewiring probabilities $p = 1, 0.2, 0.1, 0.08$. From Fig. 5, we observe that using the affinity $A^{(k)}$ in (15) at higher frequency helps improve the performance of the single-frequency class averaging nearest neighbor search algorithm, especially for the noisy graph at $p = 0.08$ (i.e., 92% of the true edges are corrupted). Moreover, combining the measures at different k 's according to (16) further improves the classification results with significant reduction of outliers at $p = 0.08$ compared to the single frequency nearest neighbor identification results.

5.2 Experiments with Simulated Cryo-EM Images

In this section, we apply multi-frequency class averaging on simulated cryo-EM projection images. For each image, the goal is to identify projection images with similar viewing directions. We simulate $N = 10,000$ clean projection images of size 129×129 pixels from a 3-D electron density map of the 70S ribosome. The orientations for the projection images are uniformly distributed over $\text{SO}(3)$. The clean images are contaminated by additive white Gaussian noise with different signal to noise ratios (SNRs). Sample images are presented in Fig. 6. Here, we do not consider the effects of contrast transfer functions (CTFs) on the images. In order to initially identify similar images and the corresponding rotational alignments, we first expand each image on steerable basis, and denoise the images by using *steerable PCA* (sPCA) [70]. Then we generate the rotationally invariant features [71] from the filtered expansion coefficients to efficiently identify nearest neighbors without performing all pairwise alignments. The optimal alignment parameters are estimated between initial nearest neighbor pairs. The initial nearest neighbor list and alignment parameters are used to construct the initial graph. For clean images, the initial graph correspond to the true neighborhood graph. For the extremely noisy images illustrated in Fig. 6, the initial similarity measure is corrupted by noise and images of totally different views can be misidentified as nearest neighbors.

In Fig. 7, we present the spectral patterns of the top eigenvalues of $\tilde{H}^{(k)}$ built from our initial neighborhood identification and rotational alignment. At high SNR, such as $\text{SNR} \geq 0.05$, we can clearly observe the multiplicities $2k + 1, 2k + 3, 2k + 5, \dots$ and the spectral gaps. As the SNR decreases, such spectral patterns start to deteriorate. When $\text{SNR} = 0.02$, the top spectral gap for frequency $k = 1$ almost disappears, while it is still noticeable for $k = 5$, which is consistent with the theoretical result that the spectral gap is more robust for larger k . Therefore, we expect that using higher k mapping $\Psi^{(k)}$ in (14) can improve single frequency class averaging.

In Fig. 8, we present the scatter plots of $A_{ij}^{(k)}$ against $(\langle \pi(x_i), \pi(x_j) \rangle + 1)^k / 2^k$, with different SNRs. Similar to the synthetic dataset, the $A_{ij}^{(k)}$'s at frequency $k = 1$ fail at low SNRs, such as $\text{SNR} = 0.02, 0.01$,

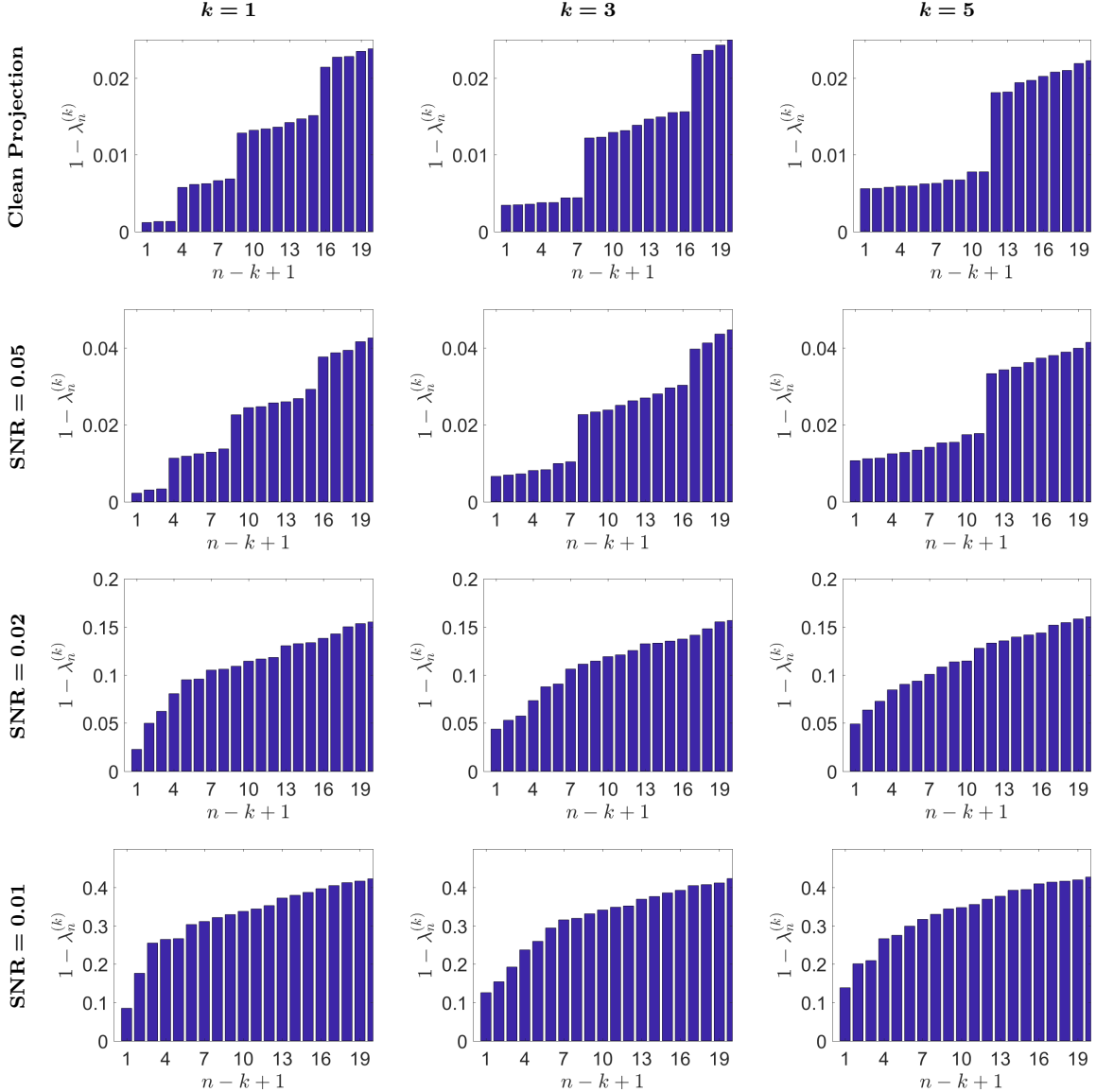


Fig. 7: Cryo-EM images: Bar plots of the top 20 eigenvalues at different frequency k and signal to noise ratio (SNR).

while the $A_{ij}^{(k)}$'s at frequency $k = 5, 10$ are still able to distinguish the images with similar viewing directions (i.e., $(\langle \pi(x_i), \pi(x_j) \rangle + 1)^k / 2^k \approx 1$). This result indicates that better neighborhood image identification can be attained using higher frequency k . Moreover, Fig. 9 shows the scatter plots of the combined affinity against the dot products $\langle \pi(x_i), \pi(x_j) \rangle$ between the true viewing angles at varying SNRs. Even at SNR = 0.01, the combined affinity A_{ij}^{All} is still able to distinguish projection images that have similar views $\pi(x)$, in contrast to the approximation results in Fig. 8.

In Fig. 10, we evaluate the results by plotting the histogram of angles between viewing directions $\arccos(\langle \pi(x_i), \pi(x_j) \rangle)$ between all identified neighboring images I_i and I_j . At high SNR, such as SNR = 0.05, using single frequency information as $k = 1, 3, 5$ can achieve similar results as combining all the frequencies; At low SNRs, such as SNR = 0.02 and 0.01, MFCA, which uses all frequencies information, outperforms the results obtained from using only a single frequency. Again, this is consistent with our expectation of the robustness of MFCA, especially in low SNR regimes. These numerical results suggest that combining different frequencies is able to extract more accurate geometric information of the dataset than one can obtain using a single frequency at $k = 1$.

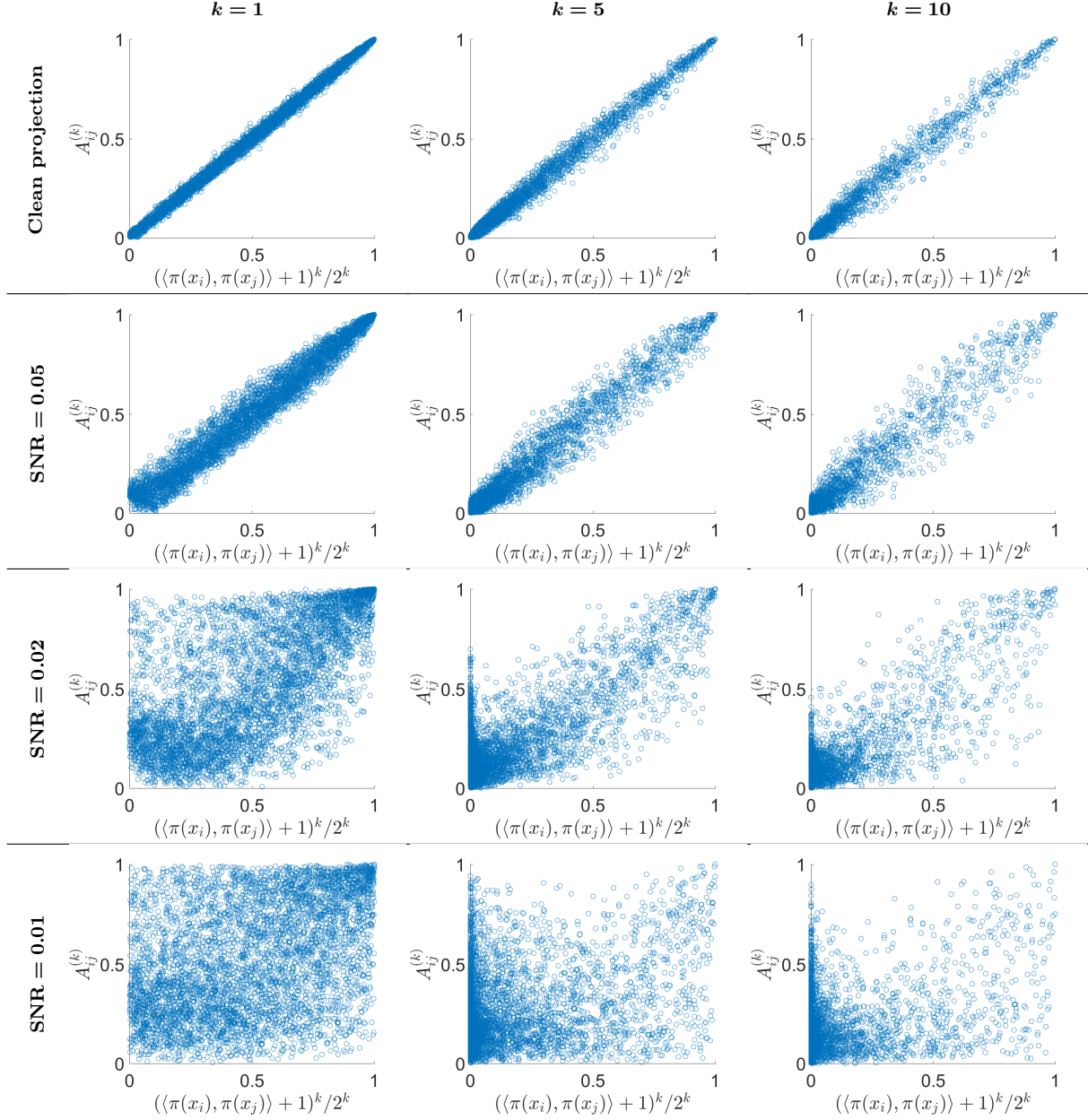


Fig. 8: Cryo-EM images: Scatter plots of $A_{ij}^{(k)}$ against $((\pi(x_i), \pi(x_j)) + 1)^k / 2^k$ for clean projections and SNR = 0.05, 0.02, 0.01, at frequency $k = 1, 5$, and 10.

6 Conclusion and Future Work

We propose in this paper a novel algorithm, referred to as multi-frequency class averaging (MFCA), for clustering noisy projection images in three-dimensional cryo-electron microscopy by the similarity among viewing directions. The new algorithm is a generalization of the eigenvector-based approach of intrinsic classification first appeared in [63, 39]. We also extended the representation theoretical framework of [38, 39] by means of explicit constructions involving the Wigner D -matrices, which completely characterizes the spectral information of a generalized localized parallel transport operator acting on sections of certain complex line bundle over the two-dimensional unit sphere in \mathbb{R}^3 ; these theoretical results conceptually establish the admissibility and (improved) stability of the new MFCA algorithm.

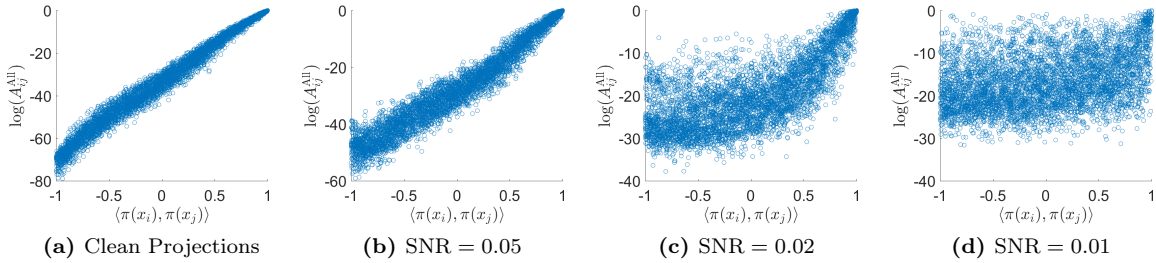


Fig. 9: Cryo-EM images: Scatter plots for log multi-frequency class averaging affinity $\log A_{ij}^{\text{all}}$ against $\langle \pi(x_i), \pi(x_j) \rangle$ for clean projections and SNR = 0.05, 0.02, 0.01.

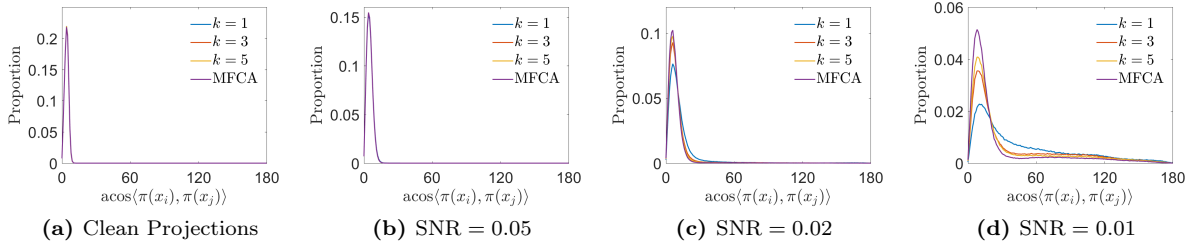


Fig. 10: Histogram of the angles (x -axis, in degrees) between the viewing directions of 10,000 simulated cryo-EM projection images and its 50 neighboring projection images, with different SNRs, from *left to right*: clean projection images, SNR = 0.05, 0.02, 0.01. Here we set the maximum frequency $k_{\text{max}} = 10$.

One intriguing future direction is to investigate into refined and more systematic aggregations of the results obtained from each individual frequency channel. Potential candidates include (1) the harmonic-retrieval-type transformations as in multi-frequency phase synchronization [34], (2) cross-frequency invariant features such as bispectrum [42, 8], and (3) tensor-based optimizations for multi-dimensional arrays [43, 58, 2]. The main idea is to further exploit the redundancy in the reconstructed information across different irreducible representations. A direct extension of the MFCA theoretical framework could be a refined geometric interpretation of the multi-frequency vector diffusion maps [26] in terms of aggregating invariant embeddings of the same underlying base manifold from multiple associated vector bundles of a fixed common principal bundle. In some sense, such a geometric model can be considered as a natural multi-view co-learning or co-training algorithm deeply rooted in semi-supervised statistical learning [9] in the unsupervised, manifold learning setup.

Another future direction of interest is to integrate the multi-frequency methodology into existing algorithmic approaches for tackling the *heterogeneity* problem in cryo-EM imaging analysis and comparative biology [3, 46, 33]. In the context of cryo-EM, this problem occurs when molecules in distinct conformations coexist in solution, and thus images collected in cryo-EM imaging from random orientations should typically be first clustered into subgroups (using e.g. the maximum likelihood classification approaches [60, 57]) before single-particle reconstruction techniques can be applied to each individual subgroup. Recent studies [17, 30, 29] even provided evidence for a continuous distribution of conformation states to present in a solution, which is far beyond the capability of maximum likelihood classification methods. We expect significant performance boost and sharper theoretical results from extensions of the multi-frequency methodology in these problems.

Acknowledgements The authors thank Shmuel Weinberger and Shamgar Gurevich for useful discussions.

Appendix A Spectral Analysis of the Localized Generalized Parallel Transport Operators

We prove Theorem 2 and Theorem 3 in this appendix.

Appendix A.1 Proof of Theorem 2

We begin with the isotypic decomposition (29), (31). Following (34), our strategy is to find a “good point” $x_0 \in \text{SO}(3)$ and a “good function” $u \in \mathcal{H}_{n,-k}$ ($n \geq |k|$) such that $u(x_0) \neq 0$, and evaluate

$$\lambda_n^{(k)}(h) = \frac{\left(T_h^{(k)} u\right)(x_0)}{u(x_0)}. \quad (51)$$

To this end, pick the following basis for the Lie algebra $\mathfrak{so}(3)$:

$$A_1 = \begin{pmatrix} 0 & 0 & 0 \\ 0 & 0 & -1 \\ 0 & 1 & 0 \end{pmatrix}, \quad A_2 = \begin{pmatrix} 0 & 0 & 1 \\ 0 & 0 & 0 \\ -1 & 0 & 0 \end{pmatrix}, \quad A_3 = \begin{pmatrix} 0 & -1 & 0 \\ 1 & 0 & 0 \\ 0 & 0 & 0 \end{pmatrix}.$$

It is straightforward to check that these elements satisfy the commutator relations

$$[A_3, A_1] = A_2, \quad [A_2, A_3] = A_1, \quad [A_1, A_2] = A_3.$$

We fix $x_0 = I_3$, the canonical standard orthonormal frame in \mathbb{R}^3 . We further equip $\text{SO}(3)$ with standard spherical coordinates — the Euler angles — of the form

$$x = x(\varphi, \vartheta, \psi) = x_0 \triangleleft e^{\varphi A_3} e^{\vartheta A_2} e^{\psi A_3}$$

where $(\varphi, \vartheta, \psi) \in (0, 2\pi) \times (0, \pi) \times (0, 2\pi)$, as in [39, §3.2.1]. The normalized Haar measure on $\text{SO}(3)$ is given by the density

$$\frac{\sin \theta}{8\pi^2} d\varphi d\vartheta d\psi.$$

Consider the subgroup T_{A_3} of $\text{SO}(3)$ generated by the infinitesimal element A_3 . For every $k \in \mathbb{Z}$ and $n \in \mathbb{N}$ with $n \geq |k|$, the Hilbert space $\mathcal{H}_{n,k}$ admits yet another isotypic decomposition with respect to the left action of T_{A_3} :

$$\mathcal{H}_{n,-k} = \bigoplus_{m=-n}^n \mathcal{H}_{n,-k}^m \quad (52)$$

where $s \in \mathcal{H}_{n,-k}^m$ if and only if

$$s(e^{-tA_3} \triangleright x) = e^{\iota m t} s(x) \quad \text{for every } x \in \text{SO}(3) \text{ and } t \in \mathbb{R}. \quad (53)$$

As pointed out in [39, §3.3.1], elements of $\mathcal{H}_{n,-k}^m$ are often referred to as (generalized) *spherical functions*. In the physics literature, they are also known as *spin-weighted spherical functions*, which are closely related with Wigner D -matrices [11, 21, 13, 36, 51]. We extend the computation in [39, §3] to $k > 1$, by fully leveraging properties of the Wigner D -matrices. In fact, we are going to fix $m = -k$ and choose the “good function” u as $D_{-k,-k}^n$, the $(-k, -k)$ th entry of the Wigner D -matrix of weight n , for any $n \geq |k|$ — it is clear from (28) that $D_{-k,-k}^n \in \mathcal{H}_{-k}$ for any $n \geq |k|$, and from (26) we know that $D_{-k,-k}^n$ satisfies (53) with $m = -k$. Our goal is to evaluate

$$\lambda_n^{(k)}(h) = \frac{\left(T_h^{(k)} D_{-k,-k}^n\right)(x_0)}{D_{-k,-k}^n(x_0)}. \quad (54)$$

Now, on the one hand we have

$$D_{-k,-k}^n(x_0) = D_{-k,-k}^n(0, 0, 0) \stackrel{(21)}{=} d_{-k,-k}^n(0) \stackrel{(25)}{=} 1. \quad (55)$$

On the other hand, note that by the invariance and equivariance of the transport data (6) we have for any $x = x(\varphi, \vartheta, \psi) \in \text{SO}(3)$

$$\begin{aligned} T^{(k)}(x_0, x) &= T^{(k)}(x_0, x_0 \triangleleft e^{\varphi A_3} e^{\vartheta A_2} e^{\psi A_3}) = T^{(k)}(x_0, e^{\varphi A_3} \triangleright x_0 \triangleleft e^{\vartheta A_2} e^{\psi A_3}) \\ &= T^{(k)}(e^{-\varphi A_3} \triangleright x_0, x_0 \triangleleft e^{\vartheta A_2} e^{\psi A_3}) = T^{(k)}(x_0 \triangleleft e^{-\varphi A_3}, x_0 \triangleleft e^{\vartheta A_2} e^{\psi A_3}) \\ &= e^{\iota \varphi} T^{(k)}(x_0, x_0 \triangleleft e^{\vartheta A_2}) e^{\iota \psi} \end{aligned}$$

and

$$D_{-k,-k}^n(x) = D_{-k,-k}^n(\varphi, \vartheta, \psi) = e^{-\iota\varphi} d_{-k,-k}^n(\vartheta) e^{-\iota\psi} = e^{-\iota\varphi} D_{-k,-k}^n(x_0 \triangleleft e^{\vartheta A_2}) e^{-\iota\psi}.$$

Therefore,

$$\begin{aligned} (T_h^{(k)} D_{-k,-k}^n)(x_0) &= \int_{B(x,a)} T^{(k)}(x_0, x) D_{-k,-k}^n(x) dx \\ &= \int_{B(x,a)} T^{(k)}(x_0, x_0 \triangleleft e^{\vartheta A_2}) D_{-k,-k}^n(x_0 \triangleleft e^{\vartheta A_2}) dx(\varphi, \vartheta, \psi) \\ &= \int_{B(x,a)} \rho_k(T(x_0, x_0 \triangleleft e^{\vartheta A_2})) D_{-k,-k}^n(x_0 \triangleleft e^{\vartheta A_2}) dx(\varphi, \vartheta, \psi) \\ &= \int_{B(x,a)} \rho_{-k}(\overline{T(x_0, x_0 \triangleleft e^{\vartheta A_2})}) D_{-k,-k}^n(x_0 \triangleleft e^{\vartheta A_2}) dx(\varphi, \vartheta, \psi) \\ &= \int_{B(x,a)} \rho_{-k}(T(x_0 \triangleleft e^{\vartheta A_2}, x_0)) D_{-k,-k}^n(x_0 \triangleleft e^{\vartheta A_2}) dx(\varphi, \vartheta, \psi) \\ &\stackrel{(*)}{=} \int_{B(x,a)} D_{-k,-k}^n((x_0 \triangleleft e^{\vartheta A_2}) \triangleleft T(x_0 \triangleleft e^{\vartheta A_2}, x_0)) dx(\varphi, \vartheta, \psi) \\ &\stackrel{(**)}{=} \int_{B(x,a)} D_{-k,-k}^n(x_0 \triangleleft e^{\vartheta A_2}) dx(\varphi, \vartheta, \psi) \end{aligned}$$

where (*) used the fact that $D_{-k,-k}^n \in \mathcal{H}_{-k}$, and (**) follows from the definition (4) and the geometric fact that $x_0 \triangleleft e^{\vartheta A_2}$ is exactly the parallel transport of x_0 along the unique geodesic connecting $\pi(x_0)$ to $\pi(x_0 \triangleleft e^{\vartheta A_2})$:

$$(x_0 \triangleleft e^{\vartheta A_2}) \triangleleft T(x_0 \triangleleft e^{\vartheta A_2}, x_0) = t_{\pi(x_0 \triangleleft e^{\vartheta A_2}), \pi(x_0)} x_0 = x_0 \triangleleft e^{\vartheta A_2}.$$

It follows that

$$\begin{aligned} (T_h^{(k)} D_{-k,-k}^n)(x_0) &= \int_{B(x,a)} D_{-k,-k}^n(x_0 \triangleleft e^{\vartheta A_2}) dx(\varphi, \vartheta, \psi) \\ &= \frac{1}{(2\pi)^2} \int_0^{2\pi} d\varphi \int_0^a \frac{\sin \vartheta}{2} D_{-k,-k}^n(0, \vartheta, 0) d\vartheta = \int_0^a \frac{\sin \vartheta}{2} d_{-k,-k}^n(\vartheta) d\vartheta. \end{aligned}$$

Since $d_{-k,-k}^n = d_{kk}^n$ (see e.g. [50, formula (3.16)]), this further implies

$$\begin{aligned} (T_h^{(k)} D_{-k,-k}^n)(x_0) &= \int_0^a \frac{\sin \vartheta}{2} d_{kk}^n(\vartheta) d\vartheta \stackrel{(24)}{=} 2^{-(k+1)} \int_0^a \sin \vartheta (1 + \cos \vartheta)^k P_{n-k}^{(0,2k)}(\cos \vartheta) d\vartheta \\ &= -2^{-(k+1)} \int_0^a (1 + \cos \vartheta)^k P_{n-k}^{(0,2k)}(\cos \vartheta) d \cos \vartheta \\ &\stackrel{z:=\cos \vartheta}{=} 2^{-(k+1)} \int_{1-h}^1 (1+z)^k P_{n-k}^{(0,2k)}(z) dz \end{aligned} \tag{56}$$

where in the last equality we used $h = 1 - \cos a$. Using the explicit form of Jacobi polynomials (see e.g. [64, Chap. IV, formula (4.2.1)])

$$\begin{aligned} P_{n-k}^{(0,2k)}(z) &= \sum_{\nu=0}^{n-k} \binom{n-k}{n-k-\nu} \binom{n+k}{\nu} \left(\frac{z-1}{2}\right)^\nu \left(\frac{z+1}{2}\right)^{n-k-\nu} \\ &= \sum_{\nu=0}^{n-k} \binom{n-k}{\nu} \binom{n+k}{\nu} \left(\frac{z-1}{2}\right)^\nu \left(\frac{z+1}{2}\right)^{n-k-\nu} \end{aligned}$$

we have

$$\begin{aligned}
\left(T_h^{(k)} D_{-k,-k}^n\right)(x_0) &= 2^{-(k+1)} \cdot 2^k \sum_{\nu=0}^{n-k} \binom{n-k}{\nu} \binom{n+k}{\nu} \int_{1-h}^1 \left(\frac{z-1}{2}\right)^\nu \left(\frac{z+1}{2}\right)^{n-\nu} dz \\
&\stackrel{z:=1-2w}{=} \frac{1}{2} \sum_{\nu=0}^{n-k} (-1)^\nu \binom{n-k}{\nu} \binom{n+k}{\nu} \int_0^{\frac{h}{2}} w^\nu (1-w)^{n-\nu} \cdot 2 dw \\
&= \sum_{\nu=0}^{n-k} (-1)^\nu \binom{n-k}{\nu} \binom{n+k}{\nu} \int_0^{\frac{h}{2}} w^\nu (1-w)^{n-\nu} dw \\
&= \sum_{\nu=0}^{n-k} (-1)^\nu \binom{n-k}{\nu} \binom{n+k}{\nu} B\left(\frac{h}{2}; \nu+1, n-\nu+1\right)
\end{aligned}$$

where $B(x; a, b) = \int_0^x w^{a-1} (1-w)^{b-1} dw$ is the incomplete Beta function. It follows that for all $n \geq |k|$

$$\begin{aligned}
\lambda_n^{(k)}(h) &= \frac{\left(T_h^{(k)} D_{-k,-k}^n\right)(x_0)}{D_{-k,-k}^n(x_0)} = \left(T_h^{(k)} D_{-k,-k}^n\right)(x_0) \\
&= \sum_{\nu=0}^{n-k} (-1)^\nu \binom{n-k}{\nu} \binom{n+k}{\nu} B\left(\frac{h}{2}; \nu+1, n-\nu+1\right).
\end{aligned}$$

From the integral form of the incomplete Beta function it is clear that $B(h/2; \nu+1, n-\nu+1)$ is a polynomial of degree $(n+1)$ in h . In particular, by repeatedly applying the recursive relation

$$B(x; a+1, b) = \frac{a}{b} B(x; a, b+1) - \frac{1}{b} x^a (1-x)^b$$

we easily obtain

$$\lambda_k^{(k)}(h) = B\left(\frac{h}{2}; 1, k+1\right) = \frac{1 - (1-h/2)^{k+1}}{k+1}, \quad (57)$$

$$\begin{aligned}
\lambda_{k+1}^{(k)}(h) &= B\left(\frac{h}{2}; 1, k+2\right) - (2k+1) B\left(\frac{h}{2}; 2, k+1\right) \\
&= B\left(\frac{h}{2}; 1, k+2\right) - \frac{2k+1}{k+1} B\left(\frac{h}{2}; 1, k+2\right) + \frac{2k+1}{k+1} \left(\frac{h}{2}\right) \left(1 - \frac{h}{2}\right)^{k+1} \\
&= -\frac{k}{k+1} \cdot \frac{1 - (1-h/2)^{k+2}}{k+2} + \frac{2k+1}{k+1} \left(\frac{h}{2}\right) \left(1 - \frac{h}{2}\right)^{k+1}, \quad (58)
\end{aligned}$$

$$\begin{aligned}
\lambda_{k+2}^{(k)}(h) &= B\left(\frac{h}{2}; 1, k+3\right) - 4(k+1) B\left(\frac{h}{2}; 2, k+2\right) + (k+1)(2k+1) B\left(\frac{h}{2}; 3, k+1\right) \\
&= B\left(\frac{h}{2}; 1, k+3\right) - 2B\left(\frac{h}{2}; 2, k+2\right) - (2k+1) \left(\frac{h}{2}\right)^2 \left(1 - \frac{h}{2}\right)^{k+1} \\
&= \frac{k}{k+2} B\left(\frac{h}{2}; 1, k+3\right) + \frac{2}{k+2} \left(\frac{h}{2}\right) \left(1 - \frac{h}{2}\right)^{k+2} - (2k+1) \left(\frac{h}{2}\right)^2 \left(1 - \frac{h}{2}\right)^{k+1} \\
&= \frac{k}{k+2} \cdot \frac{1 - (1-h/2)^{k+3}}{k+3} + \frac{2}{k+2} \left(\frac{h}{2}\right) \left(1 - \frac{h}{2}\right)^{k+2} - (2k+1) \left(\frac{h}{2}\right)^2 \left(1 - \frac{h}{2}\right)^{k+1}, \quad (59)
\end{aligned}$$

which give rise to (36) and (37).

It now remains to compute a quadratic approximation for $\lambda_n^{(k)}(h)$ for $h \rightarrow 0$, for all $n \geq |k|$. This can be done by direct computation using the integral form of the incomplete beta function: for all $n \geq |k|$,

$$\lambda_n^{(k)}(0) = 0, \quad (60)$$

$$\partial_h \lambda_n^{(k)}(0) = \sum_{\nu=0}^{n-k} (-1)^\nu \binom{n-k}{\nu} \binom{n+k}{\nu} \cdot \frac{1}{2} \left(\frac{h}{2}\right)^\nu \left(1 - \frac{h}{2}\right)^{n-\nu} \Big|_{h=0} = \frac{1}{2}, \quad (61)$$

$$\begin{aligned} \partial_h^2 \lambda_n^{(k)}(0) &= \sum_{\nu=1}^{n-k} (-1)^\nu \binom{n-k}{\nu} \binom{n+k}{\nu} \cdot \frac{\nu}{4} \left(\frac{h}{2}\right)^{\nu-1} \left(1 - \frac{h}{2}\right)^{n-\nu} \Big|_{h=0} \\ &\quad + \sum_{\nu=0}^{n-k} (-1)^\nu \binom{n-k}{\nu} \binom{n+k}{\nu} \cdot \frac{-(n-\nu)}{4} \left(\frac{h}{2}\right)^\nu \left(1 - \frac{h}{2}\right)^{n-\nu-1} \Big|_{h=0} \\ &= -\frac{1}{4} (n-k)(n+k) - \frac{n}{4} = -\frac{1}{4} (n^2 + n - k^2) \end{aligned} \quad (62)$$

and (35) follows from the Taylor expansion

$$\lambda_n^{(k)}(h) = \lambda_n^{(k)}(0) + h \partial_h \lambda_n^{(k)}(0) + \frac{h^2}{2} \partial_h^2 \lambda_n^{(k)}(0) + O(h^3).$$

This completes the entire proof of Theorem 2. \square

Appendix A.2 Proof of Theorem 3

Lemma 1 (1) *There exists $h_1^{(k)} \in (0, 2]$ such that $\lambda_n^{(k)}(h) \leq \lambda_k^{(k)}(h)$ for every $n \geq k+1$ and $h \in (0, h_1^{(k)})$.*
(2) *There exists $h_2^{(k)} \in (0, 2]$ such that $\lambda_n^{(k)}(h) \leq \lambda_{k+1}^{(k)}(h)$ for every $n \geq k+2$ and $h \in (0, h_2^{(k)})$.*

Proof (Proof of Lemma 1) Since $\lambda_n^{(k)}(0) = 0$ for all $k \in \mathbb{Z}$ and $n \geq |k|$, we will just compare the first order derivatives $\partial_h \lambda_n^{(k)}(h)$ over an interval with 0 as the left end point. By (56), $\partial_h \lambda_n^{(k)}(h)$ admits a closed form expression in terms of Jacobi polynomials:

$$\partial_h \lambda_n^{(k)}(h) = \frac{1}{2} \left(1 - \frac{h}{2}\right)^k P_{n-k}^{(0,2k)}(1-h) \stackrel{h=\cos a}{=} \frac{1}{2} \left(\frac{1+\cos a}{2}\right)^k P_{n-k}^{(0,2k)}(\cos a).$$

In particular, under change-of-coordinates $h = 1 - \cos a$ we have

$$\begin{aligned} \partial_h \lambda_k^{(k)}(h) &= \frac{1}{2} \left(\frac{1+\cos a}{2}\right)^k P_0^{(0,2k)}(\cos a) = \frac{1}{2} \left(\frac{1+\cos a}{2}\right)^k, \\ \partial_h \lambda_{k+1}^{(k)}(h) &= \frac{1}{2} \left(\frac{1+\cos a}{2}\right)^k P_1^{(0,2k)}(\cos a) = \frac{1}{2} \left(\frac{1+\cos a}{2}\right)^k [1 - (k+1)(1 - \cos a)]. \end{aligned}$$

it is clear that $0 < \partial_h \lambda_{k+1}^{(k)}(h) < \partial_h \lambda_k^{(k)}(h)$ for all $h = 1 - \cos a \in (0, 1/(k+1)]$, which together with $\lambda_k^{(k)}(0) = \lambda_{k+1}^{(k)}(0)$ gives rise to

$$\lambda_{k+1}^{(k)}(h) \leq \lambda_k^{(k)}(h) \quad \text{for all } 0 < h \leq \frac{1}{k+1}. \quad (63)$$

With (63), the proof of both (1) and (2) of Lemma 1 is reduced to only the part (2) of Lemma 1. The remaining of this proof is devoted to establishing (2) of Lemma 1.

By the classical result of Szegő [64, Theorem 8.21.13], there exists a fixed positive number $c > 0$ such that

$$P_{n-k}^{(0,2k)}(\cos \theta) = \frac{1}{\sqrt{n}} k(\theta) \left[\cos(N\theta + \gamma) + (n \sin \theta)^{-1} O(1) \right], \quad \text{for all } \frac{c}{n} \leq \theta \leq \pi - \frac{c}{n} \quad (64)$$

where

$$k(\theta) = \frac{1}{\sqrt{\pi \sin(\theta/2) \cos(\theta/2) \cdot [\cos(\theta/2)]^{2k}}} = \left(\frac{2}{1+\cos \theta}\right)^k \sqrt{\frac{2}{\pi \sin \theta}},$$

$$N = n + \frac{2k+1}{2}, \quad \lambda = -\frac{\pi}{4}.$$

In particular, by making the $O(1)$ term in (64) explicit, we have for some absolute constant $C > 0$

$$\left(\frac{1+\cos\theta}{2}\right)^k \left|P_{n-k}^{(0,2k)}(\cos\theta)\right| \leq \sqrt{\frac{2}{n\pi}} \cdot \frac{1}{\sqrt{\sin\theta}} \left(1 + \frac{C}{n\sin\theta}\right) \quad \text{for all } \frac{c}{n} \leq \theta \leq \pi - \frac{c}{n}. \quad (65)$$

Note that the left hand side is precisely the absolute value of $2\partial_h \lambda_n^{(k)}(h) = 2\partial_h \lambda_n^{(k)}(1 - \cos\theta)$. We seek an upper bound for the right hand side of (65) that holds uniformly for all sufficiently large n . To this end, consider the largest zero of $P_{n-k}^{(0,2k)}(x)$ for $x \in [-1, 1]$, denoted as $x_{n-k}^* = \cos a_{n-k}^*$ (thus a_{n-k}^* is the smallest zero of the function $\alpha \mapsto P_{n-k}^{(0,2k)}(\cos\alpha)$ on $\alpha \in [0, \pi]$). Well-known estimates for the extreme zero of Jacobi polynomials (see e.g. [20, §2.2]) indicates

$$x_{n-k}^* > 1 - O\left(\frac{1}{n^2}\right) \text{ as } n \rightarrow \infty \quad \Rightarrow \quad a_{n-k}^* \rightarrow 0 \text{ as } n \rightarrow \infty$$

thus for any $\epsilon_1 > 0$ there exists $N_1 > 0$ such that for all sufficiently large $n \geq N_1$ we have

$$\sin a_{n-k}^* \geq (1 - \epsilon_1) a_{n-k}^* \quad (66)$$

since $\lim_{x \rightarrow 0} (\sin x)/x = 1$. In the meanwhile, [23, Theorem 3.1] bounds $x_{n-k}^* = \cos a_{n-k}^*$ from above by

$$x_{n-k}^* < \frac{\left(2k + \frac{1}{2}\right)^2 + 4(n-k)\left(n + k + \frac{1}{2}\right)}{(2n - 2k + 1 + 2k)^2} = \frac{4n^2 + 2n + 1/4}{(2n + 1)^2} = 1 - \frac{2n + 3/4}{(2n + 1)^2}. \quad (67)$$

Using the elementary inequality $1 - x^2/2 \leq \cos x$ for $x \in [0, 2]$, (67) leads to

$$1 - \frac{(a_{n-k}^*)^2}{2} \leq \cos a_{n-k}^* = x_{n-k}^* < 1 - \frac{2n + 3/4}{(2n + 1)^2} \quad \Rightarrow \quad a_{n-k}^* > \sqrt{\frac{4n + 3/2}{(2n + 1)^2}} \rightarrow \frac{1}{\sqrt{n}} \text{ as } n \rightarrow \infty$$

which further implies (1) for sufficiently large n , $a_{n-k}^* \in [c/n, \pi - c/n]$, and (2) by choosing n sufficiently large we can ensure for the same arbitrary $\epsilon_1 > 0$ chosen for (66), that, in addition to (66), there holds

$$a_{n-k}^* > \frac{1 - \epsilon_1}{\sqrt{n}}. \quad (68)$$

Now consider the smallest local extremum μ_{n-k}^* of the function $P_{n-k}^{(0,2k)}(\cos\alpha)$ for $\alpha \in [0, \pi]$ that is larger than a_{n-k}^* , i.e.,

$$\mu_{n-k}^* := \min \left\{ \alpha \in [0, \pi] \mid \partial_\alpha P_{n-k}^{(0,2k)}(\cos\alpha) = 0 \text{ and } \alpha \geq a_{n-k}^* \right\}$$

which by (68) is guaranteed to fall within $[c/n, \pi - c/n]$. For any $n \geq N_0$, by (65), (66), and (68), we have

$$\begin{aligned} \left(\frac{1+\cos\mu_{n-k}^*}{2}\right)^k \left|P_{n-k}^{(0,2k)}(\cos\mu_{n-k}^*)\right| &\leq \sqrt{\frac{2}{\pi n}} \cdot \frac{1}{\sqrt{\sin\mu_{n-k}^*}} \left(1 + \frac{C}{n\sin\mu_{n-k}^*}\right) \\ &\leq \sqrt{\frac{2}{\pi n}} \cdot \frac{1}{\sqrt{\sin a_{n-k}^*}} \left(1 + \frac{C}{n\sin a_{n-k}^*}\right) \\ &\leq \sqrt{\frac{2}{\pi n}} \cdot \frac{1}{\sqrt{(1 - \epsilon_1) a_{n-k}^*}} \left(1 + \frac{C}{n(1 - \epsilon_1) a_{n-k}^*}\right) \\ &< \frac{1}{(1 - \epsilon_1) n^{\frac{1}{4}}} \sqrt{\frac{2}{\pi}} \left(1 + \frac{C}{(1 - \epsilon_1)^2 \sqrt{n}}\right). \end{aligned}$$

The same inequality holds if we replace μ_{n-k}^* with any other extremum of the function $\alpha \mapsto P_{n-k}^{(0,2k)}(\cos \alpha)$ in $\alpha \in [c/n, \pi - c/n]$. In particular, this implies that for all sufficiently large n we have (recalling that $h = 1 - \cos a$)

$$\partial_h \lambda_n^{(k)}(h) = \partial_h \lambda_n^{(k)}(1 - \cos a) \leq \frac{1}{2} \left(\frac{1 + \cos a}{2} \right)^k \left| P_{n-k}^{(0,2k)}(\cos a) \right| < \frac{1}{4} \quad \text{for all } a \in [c/n, \pi - c/n].$$

The rest of the proof follows easily from the proof of [39, Theorem 4]: Let $a_0 \in (0, \pi)$ be such that

$$\partial_h \lambda_{k+1}^{(k)}(h) = \partial_h \lambda_{k+1}^{(k)}(1 - \cos a) = \frac{1}{2} \left(\frac{1 + \cos a}{2} \right)^k [1 - (k+1)(1 - \cos a)] > \frac{1}{4}$$

for all $a < a_0$ and sufficiently large n ; the remaining finitely cases can be verified directly as claimed in [39, §A.2.1, pp. 612]. Note that such a value a_0 exists because when $a = 0$ (i.e., $h = 1$)

$$\partial_h \lambda_{k+1}^{(k)}(1) = \frac{1}{2} > \frac{1}{4}.$$

As argued in [39, §A.2, pp. 611], we set $z_0 = \cos a_0$ and $h_1^{(k)} = h_2^{(k)} = 1 + z_0$, which ensures $\partial_h \lambda_n^{(k)}(z) \leq \partial_h \lambda_{k+1}^{(k)}(z)$ for all $z \in [-1, z_0]$, and furthermore $\lambda_n^{(k)}(h) \leq \lambda_{k+1}^{(k)}(h)$, for all $n \geq k+1$. This proves (2) of Lemma 1 and completes the entire proof of Lemma 1. \square

Lemma 2 (1) *There exists $N_1^{(k)} > 0$ such that $\lambda_n^{(k)}(h) \leq \lambda_k^{(k)}(h)$ for every $n \geq N_1^{(k)}$ and $h \in [h_1^{(k)}, 2]$.*
(2) *There exists $N_2^{(k)} > 0$ such that $\lambda_n^{(k)}(h) \leq \lambda_k^{(k)}(h)$ for every $n \geq N_2^{(k)}$ and $h \in [h_2^{(k)}, 1/(k+1)]$.*

Proof (Proof of Lemma 2) First note, on the one hand, that the Schatten 2-norm of $T_h^{(k)}$ can be easily computed: By [55, Theorem VI.23],

$$\begin{aligned} \|T_h^{(k)}\|_2^2 &= \int_{\text{SO}(3)} \int_{\text{SO}(3)} \left| T_h^{(k)}(x, y) \right|^2 dx dy = \int_{\text{SO}(3)} \int_{B(y, a)} \left| T_h^{(k)}(x, y) \right|^2 dx dy \\ &= \int_{\text{SO}(3)} \int_{B(y, a)} dx dy = \int_0^a \frac{\sin \vartheta}{2} d\vartheta = \frac{1 - \cos \vartheta}{2} = \frac{h}{2} \end{aligned}$$

where the last equality follows from $h = 1 - \cos a$. On the other hand,

$$\|T_h^{(k)}\|_2^2 = \sum_{n=k}^{\infty} (2n+1) \left(\lambda_n^{(k)} \right)^2$$

which gives the same bound as [39, formula (A.4)]:

$$\lambda_n^{(k)}(h) \leq \frac{\sqrt{h}}{\sqrt{4n+2}}.$$

Since by (57) we have

$$\lambda_k^{(k)}(h) = \frac{1 - (1 - h/2)^{k+1}}{k+1} \geq \frac{1 - \left(1 - h_1^{(k)}/2\right)^{k+1}}{k+1} \quad \text{for all } h \in [h_1^{(k)}, 2],$$

it is straightforward to verify by direct computation that there exists $N_1^{(k)} > 0$ such that $\sqrt{h}/\sqrt{4n+2} \leq \lambda_k^{(k)}(h)$ for every $n \geq N_1^{(k)}$ and $h \in [h_1^{(k)}, 2]$. This proves (1) of Lemma 2. Furthermore, by (58)

$$\lambda_{k+1}^{(k)}(h) = -\frac{k}{k+1} \cdot \frac{1 - (1 - h/2)^{k+2}}{k+2} + \frac{2k+1}{k+1} \left(\frac{h}{2} \right) \left(1 - \frac{h}{2} \right)^{k+1}$$

a direct computation for the derivative of the left hand side with respect to h gives

$$\partial_h \lambda_{k+1}^{(k)}(h) = \frac{1}{2} [1 - (k+1)h] \left(1 - \frac{h}{2} \right)^k$$

from which it is easy to directly verify that $h \mapsto \lambda_{k+1}^{(k)}(h)$ achieves its maximum at $h = 1/(k+1)$ over $h \in [0, 2]$, and $\lambda_{k+1}^{(k)}(h) > 0$ for all $h \in [0, 1/(k+1)]$. It is then easy to verify by direct computation that there exists $N_2^{(k)}$ such that $\sqrt{h}/\sqrt{4n+2} \leq \lambda_{k+1}^{(k)}(h)$ for every $n \geq N_2^{(k)}$ and $h \in [h_2^{(k)}, 1/(k+1)]$. This proves (2) of Lemma 2. \square

Proof (Proof of Theorem 3) Direct computation using (57) and (58) establishes (38):

$$\begin{aligned} G^{(k)}(h) &= \lambda_k^{(k)}(h) - \lambda_{k+1}^{(k)}(h) = \frac{1}{2} \int_1^{1-h} \left[(1+z)^k \frac{1}{2^k} - (1+z)^{k+1} \frac{1}{2^{k+1}} + (2k+1)(1+z)^k(1-z) \frac{1}{2^{k+1}} \right] dz \\ &= \frac{1}{2^{k+1}} \int_1^{1-h} (1+z)^k \left(1 - \frac{1+z}{2} + \frac{(2k+1)(1-z)}{2} \right) dz = \frac{1}{2^{k+1}} \int_1^{1-h} (1-z)(1+z)^k dz \\ &= \frac{(z+1)^{k+1}(k(z-1)+z-3)}{2^{k+1}(k+2)} = \frac{2^{k+2} - (2-h)^{k+1}((k+1)h+2)}{2^{k+1}(k+2)}. \end{aligned}$$

Unsurprisingly, the spectral gap depends on the “frequency channel” parameter $k \in \mathbb{N}$. The rest of the proof follows verbatim the proof of [39, Theorem 4]: By Lemma 1 and Lemma 2 we have $\lambda_n^{(k)} \leq \lambda_k^{(k)}(k)$ for every $n \geq N_1^{(k)}$ and $h \in [0, 2]$, as well as $\lambda_n^{(k)} \leq \lambda_{k+1}^{(k)}(k)$ for every $n \geq N_2^{(k)}$ and $h \in [0, 1/(k+1)]$. We then verify directly both $\lambda_n^{(k)} \leq \lambda_k^{(k)}(h)$ over $h \in [0, 2]$ and $\lambda_n^{(k)} \leq \lambda_{k+1}^{(k)}(h)$ over $h \in [0, 1/(k+2)]$ for the finitely many cases left ($k \leq n \leq N_1^{(k)}$ and $k+1 \leq n \leq N_2^{(k)}$, respectively). \square

Remark 4 A similar direct computation can be done to compute the gap between $\lambda_{k+1}^{(k)}(h)$ and $\lambda_{k+2}^{(k)}(h)$:

$$H^{(k)}(h) = \lambda_{k+1}^{(k)}(h) - \lambda_{k+2}^{(k)}(h) = \frac{2^{k+2} - (2-h)^{k+1}((k+1)h+2)}{2^{k+1}(k+2)}.$$

Note that $H^{(k)}(h)$ dominates $G^{(k)}(h)$ and becomes the main “spectral gap” as $h \rightarrow 2$.

References

1. Abbe, E., Fan, J., Wang, K., Zhong, Y.: Entrywise eigenvector analysis of random matrices with low expected rank. arXiv preprint arXiv:1709.09565 (2017)
2. Ankele, M., Lim, L.H., Groeschel, S., Schultz, T.: Versatile, robust, and efficient tractography with constrained higher-order tensor fofds. *International Journal of Computer Assisted Radiology and Surgery* **12**(8), 1257–1270 (2017). DOI 10.1007/s11548-017-1593-6
3. Bajaj, C., Gao, T., He, Z., Huang, Q., Liang, Z.: SMAC: Simultaneous mapping and clustering using spectral decompositions. In: *International Conference on Machine Learning*, pp. 334–343 (2018)
4. Bandeira, A.S., Chen, Y., Singer, A.: Non-unique games over compact groups and orientation estimation in cryo-EM. arXiv preprint arXiv:1505.03840 (2015)
5. Bandeira, A.S., Singer, A., Spielman, D.A.: A Cheeger Inequality for the Graph Connection Laplacian. *SIAM Journal on Matrix Analysis and Applications* **34**(4), 1611–1630 (2013)
6. Belkin, M., Niyogi, P.: Towards a Theoretical Foundation for Laplacian-Based Manifold Methods. In: *Learning Theory*, pp. 486–500. Springer (2005)
7. Belkin, M., Niyogi, P.: Convergence of Laplacian Eigenmaps. *Advances in Neural Information Processing Systems* **19**, 129 (2007)
8. Bendory, T., Boumal, N., Ma, C., Zhao, Z., Singer, A.: Bispectrum inversion with application to multireference alignment. *Trans. Sig. Proc.* **66**(4), 1037–1050 (2018). DOI 10.1109/TSP.2017.2775591. URL <https://doi.org/10.1109/TSP.2017.2775591>
9. Blum, A., Mitchell, T.: Combining labeled and unlabeled data with co-training. In: *Proceedings of the Eleventh Annual Conference on Computational Learning Theory, COLT’ 98*, pp. 92–100. ACM, New York, NY, USA (1998). DOI 10.1145/279943.279962
10. Boumal, N., Singer, A., Absil, P.A., Blondel, V.D.: Cramér–Rao Bounds for Synchronization of Rotations. *Information and Inference* **3**(1), 1–39 (2014)
11. Boyle, M.: How should spin-weighted spherical functions be defined? *Journal of Mathematical Physics* **57**(9), 092504 (2016)
12. Bröcker, T., Tom Dieck, T.: *Representations of compact Lie groups*, vol. 98. Springer Science & Business Media (2013)
13. Campbell, W.B.: Tensor and spinor spherical harmonics and the spin-s harmonics $\text{sym}(\theta, \varphi)$. *Journal of Mathematical Physics* **12**(8), 1763–1770 (1971)
14. Chen, B., Frank, J.: Two promising future developments of cryo-EM: capturing short-lived states and mapping a continuum of states of a macromolecule. *Microscopy* **65**(1), 69–79 (2015). DOI 10.1093/jmicro/dfv344. URL <https://doi.org/10.1093/jmicro/dfv344>

15. Chow, Y., Gatteschi, L., Wong, R.: A bernstein-type inequality for the jacobi polynomial. *Proceedings of the American Mathematical Society* **121**(3), 703–709 (1994)
16. Coifman, R.R., Lafon, S.: Diffusion maps. *Applied and computational harmonic analysis* **21**(1), 5–30 (2006)
17. Dashti, A., Schwander, P., Langlois, R., Fung, R., Li, W., Hosseinizadeh, A., Liao, H.Y., Pallesen, J., Sharma, G., Stupina, V.A., Simon, A.E., Dinman, J.D., Frank, J., Ourmazd, A.: Trajectories of the ribosome as a Brownian nanomachine. *Proceedings of the National Academy of Sciences of the United States of America* **111**(49), 17492–7 (2014)
18. Davis, C., Kahan, W.: The rotation of eigenvectors by a perturbation. iii. *SIAM Journal on Numerical Analysis* **7**(1), 1–46 (1970). DOI 10.1137/0707001
19. Doyle, D.A., Cabral, J.M., Pfuetzner, R.A., Kuo, A., Gulbis, J.M., Cohen, S.L., Chait, B.T., MacKinnon, R.: The structure of the potassium channel: Molecular basis of k⁺ conduction and selectivity. *Science* **280**(5360), 69–77 (1998). DOI 10.1126/science.280.5360.69
20. Driver, K.A., Jordaan, K.: Bounds for extreme zeros of some classical orthogonal polynomials. *Journal of Approximation Theory* **164**(9), 1200–1204 (2012). DOI <https://doi.org/10.1016/j.jat.2012.05.014>. URL <http://www.sciencedirect.com/science/article/pii/S0021904512001050>
21. Eastwood, M., Tod, P.: Edth – a differential operator on the sphere. *Mathematical Proceedings of the Cambridge Philosophical Society* **92**(2), 317–330 (1982)
22. El Karoui, N., Wu, H.T.: Graph connection laplacian methods can be made robust to noise. *Ann. Statist.* **44**(1), 346–372 (2016). DOI 10.1214/14-AOS1275
23. Elbert, A., Laforgia, A., Rodonò, L.G.: On the zeros of jacobi polynomials. *Acta Mathematica Hungarica* **64**(4), 351–359 (1994)
24. Eldridge, J., Belkin, M., Wang, Y.: Unperturbed: spectral analysis beyond Davis-Kahan. arxiv preprint. arxiv: 1706.06516 (2017). URL <http://arxiv.org/abs/1706.06516>
25. Fan, J., Wang, W., Zhong, Y.: An ℓ_∞ Eigenvector Perturbation Bound and Its Application. *Journal of Machine Learning Research* **18**(207), 1–42 (2018). URL <http://jmlr.org/papers/v18/16-140.html>
26. Fan, Y., Zhao, Z.: Cryo-electron microscopy image analysis using multi-frequency vector diffusion maps. arXiv preprint arXiv:1904.07772 (2019)
27. Fan, Y., Zhao, Z.: Multi-frequency vector diffusion maps. In: K. Chaudhuri, R. Salakhutdinov (eds.) *Proceedings of the 36th International Conference on Machine Learning, Proceedings of Machine Learning Research*, vol. 97, pp. 1843–1852. PMLR, Long Beach, California, USA (2019). URL <http://proceedings.mlr.press/v97/fan19a.html>
28. Frank, J.: *Three-dimensional electron microscopy of macromolecular assemblies: visualization of biological molecules in their native state*. Oxford University Press (2006)
29. Frank, J.: New Opportunities Created by Single-Particle Cryo-EM: The Mapping of Conformational Space. *Biochemistry* **57**(6), 888–888 (2018). DOI 10.1021/acs.biochem.8b00064
30. Frank, J., Ourmazd, A.: Continuous changes in structure mapped by manifold embedding of single-particle data in cryo-EM. *Methods* **100**, 61–67 (2016). DOI 10.1016/J.YMETH.2016.02.007
31. Gao, T.: *Hypoelliptic Diffusion Maps and Their Applications in Automated Geometric Morphometrics*. Ph.D. thesis, Duke University (2015)
32. Gao, T.: *The Diffusion Geometry of Fibre Bundles: Horizontal Diffusion Maps*. submitted (2016). ArXiv:1602.02330
33. Gao, T., Brodzki, J., Mukherjee, S.: The geometry of synchronization problems and learning group actions. *Discrete & Computational Geometry* (2019). DOI 10.1007/s00454-019-00100-2. URL <https://doi.org/10.1007/s00454-019-00100-2>
34. Gao, T., Zhao, Z.: Multi-frequency phase synchronization. In: K. Chaudhuri, R. Salakhutdinov (eds.) *Proceedings of the 36th International Conference on Machine Learning, Proceedings of Machine Learning Research*, vol. 97, pp. 2132–2141. PMLR, Long Beach, California, USA (2019). URL <http://proceedings.mlr.press/v97/gao19f.html>
35. Gelfand, I.M., Minlos, R.A., Shapiro, Z.Y.: *Representations of the Rotation and Lorentz Groups and their Applications*. Courier Dover Publications (2018)
36. Goldberg, J.N., MacFarlane, A.J., Newman, E.T., Rohrlich, F., Sudarshan, E.G.: Spin-s spherical harmonics and δ . *Journal of Mathematical Physics* **8**(11), 2155–2161 (1967)
37. Haagerup, U., Schlichtkrull, H.: Inequalities for Jacobi polynomials. *The Ramanujan Journal* **33**(2), 227–246 (2014). DOI 10.1007/s11139-013-9472-4. URL <https://doi.org/10.1007/s11139-013-9472-4>
38. Hadani, R., Singer, A.: Representation Theoretic Patterns in Three Dimensional Cryo-Electron Microscopy I: The Intrinsic Reconstruction Algorithm. *Annals of Mathematics* **174**(2), 1219–1241 (2011)
39. Hadani, R., Singer, A.: Representation theoretic patterns in three-dimensional cryo-electron microscopy II – the class averaging problem. *Foundations of computational mathematics* **11**(5), 589–616 (2011)
40. Heel, M.V.: Angular reconstruction: A posteriori assignment of projection directions for 3d reconstruction. *Ultramicroscopy* **21**(2), 111–123 (1987). DOI [https://doi.org/10.1016/0304-3991\(87\)90078-7](https://doi.org/10.1016/0304-3991(87)90078-7)
41. Henderson, R., McMullan, G.: Problems in obtaining perfect images by single-particle electron cryomicroscopy of biological structures in amorphous ice. *Microscopy* **62**(1), 43–50 (2013). DOI 10.1093/jmicro/dfs094. URL <https://doi.org/10.1093/jmicro/dfs094>
42. Kakarala, R.: The bispectrum as a source of phase-sensitive invariants for fourier descriptors: A group-theoretic approach. *Journal of Mathematical Imaging and Vision* **44**(3), 341–353 (2012). DOI 10.1007/s10851-012-0330-6. URL <https://doi.org/10.1007/s10851-012-0330-6>
43. Kolda, T., Bader, B.: Tensor decompositions and applications. *SIAM Review* **51**(3), 455–500 (2009). DOI 10.1137/07070111X
44. Koltchinskii, V., Giné, E.: Random Matrix Approximation of Spectra of Integral Operators. *Bernoulli* **6**(1), 113–167 (2000). URL <https://projecteuclid.org:443/euclid.bj/1082665383>
45. Koornwinder, T., Kostenko, A., Teschl, G.: Jacobi polynomials, bernstein-type inequalities and dispersion estimates for the discrete laguerre operator. *Advances in Mathematics* **333**, 796–821 (2018)
46. Lederman, R.R., Singer, A.: *A Representation Theory Perspective on Simultaneous Alignment and Classification*. arxiv preprint (2016)

47. Lin, C.Y., Minasian, A., Qi, X.J., Wu, H.T.: Manifold learning via the principle bundle approach. *Frontiers in Applied Mathematics and Statistics* **4**, 21 (2018). DOI 10.3389/fams.2018.00021
48. MacKinnon, R.: Potassium channels and the atomic basis of selective ion conduction (nobel lecture). *Angewandte Chemie International Edition* **43**(33), 4265–4277 (2004)
49. Malyarenko, A.: Invariant random fields in vector bundles and application to cosmology. *Annales de l’I.H.P. Probabilités et statistiques* **47**(4), 1068–1095 (2011). DOI 10.1214/10-AIHP409. URL http://www.numdam.org/item/AIHPB_2011__47_4_1068_0
50. Marinucci, D., Peccati, G.: Random fields on the sphere: representation, limit theorems and cosmological applications, vol. 389. Cambridge University Press (2011)
51. Newman, E.T., Penrose, R.: Note on the bondi-metzner-sachs group. *Journal of Mathematical Physics* **7**(5), 863–870 (1966)
52. Oikonomou, C.M., Jensen, G.J.: The development of cryo-em and how it has advanced microbiology. *Nature microbiology* **2**(12), 1577–1579 (2017)
53. Penczek, P.A., Zhu, J., Frank, J.: A common-lines based method for determining orientations for $n > 3$ particle projections simultaneously. *Ultramicroscopy* **63**(3-4), 205–218 (1996)
54. Perry, A., Wein, A.S., Bandeira, A.S., Moitra, A.: Message-Passing Algorithms for Synchronization Problems over Compact Groups. *Communications on Pure and Applied Mathematics* (2018)
55. Reed, M., Simon, B.: *Methods of modern mathematical physics. vol. 1. Functional analysis.* Academic San Diego (1980)
56. Salas, D., Le Gall, A., Fiche, J.B., Valeri, A., Ke, Y., Bron, P., Bellot, G., Nollmann, M.: Angular reconstitution-based 3d reconstructions of nanomolecular structures from superresolution light-microscopy images. *Proceedings of the National Academy of Sciences* (2017). DOI 10.1073/pnas.1704908114. URL <https://www.pnas.org/content/early/2017/08/14/1704908114>
57. Scheres, S.H.: A Bayesian View on Cryo-EM Structure Determination. *Journal of Molecular Biology* **415**(2), 406–418 (2012). DOI 10.1016/J.JMB.2011.11.010
58. Schultz, T., Fuster, A., Ghosh, A., Deriche, R., Florack, L., Lim, L.H.: Higher-order tensors in diffusion imaging. In: C.F. Westin, A. Vilanova, B. Burgeth (eds.) *Visualization and Processing of Tensors and Higher Order Descriptors for Multi-Valued Data*, pp. 129–161. Springer Berlin Heidelberg, Berlin, Heidelberg (2014)
59. Shkolnisky, Y., Singer, A.: Viewing Direction Estimation in Cryo-EM using Synchronization. *SIAM Journal on Imaging Sciences* **5**(3), 1088–1110 (2012)
60. Sigworth, F.J., Doerschuk, P.C., Carazo, J.M., Scheres, S.H.W.: An Introduction to Maximum-Likelihood Methods in Cryo-EM. In: *Methods in enzymology*, vol. 482, pp. 263–294. San Diego, CA (United States); Academic Press Inc. (2010). DOI 10.1016/S0076-6879(10)82011-7
61. Singer, A.: Angular Synchronization by Eigenvectors and Semidefinite Programming. *Applied and Computational Harmonic Analysis* **30**(1), 20–36 (2011). DOI 10.1016/j.acha.2010.02.001
62. Singer, A., Wu, H.T.: Vector Diffusion Maps and the Connection Laplacian. *Communications on Pure and Applied Mathematics* **65**(8), 1067–1144 (2012)
63. Singer, A., Zhao, Z., Shkolnisky, Y., Hadani, R.: Viewing angle classification of cryo-electron microscopy images using eigenvectors. *SIAM Journal on Imaging Sciences* **4**(2), 723–759 (2011)
64. Szegő, G.: Orthogonal polynomials, vol. 23. American Mathematical Soc. (1939)
65. Vainshtein, B., Goncharov, A.: Determination of the spatial orientation of arbitrarily arranged identical particles of unknown structure from their projections. In: *Soviet Physics Doklady*, vol. 31, p. 278 (1986)
66. Varshalovich, D.A., Moskalev, A.N., Khersonskii, V.K.: *Quantum theory of angular momentum.* World Scientific (1988)
67. Wang, L., Singer, A.: Exact and Stable Recovery of Rotations for Robust Synchronization. *Information and Inference* (2013). DOI 10.1093/imaiai/iat005
68. Ye, K., Lim, L.H.: Cohomology of Cryo-Electron Microscopy. *SIAM Journal on Applied Algebra and Geometry* **1**(1), 507–535 (2017). DOI 10.1137/16M1070220
69. Yu, Y., Wang, T., Samworth, R.J.: A useful variant of the davis–kahan theorem for statisticians. *Biometrika* **102**(2), 315–323 (2014)
70. Zhao, Z., Shkolnisky, Y., Singer, A.: Fast steerable principal component analysis. *IEEE transactions on computational imaging* **2**(1), 1–12 (2016)
71. Zhao, Z., Singer, A.: Rotationally invariant image representation for viewing direction classification in cryo-em. *Journal of structural biology* **186**(1), 153–166 (2014)
72. Zhong, Y., Boumal, N.: Near-Optimal Bounds for Phase Synchronization. *SIAM Journal on Optimization* **28**(2), 989–1016 (2018). DOI 10.1137/17M1122025